2013

Fuel-Efficient Feedback Control of Orbital Motion Around Irregular-Shaped Asteroids

Tim Winkler
Iowa State University

Fuel-efficient feedback control of orbital motion around irregular-shaped asteroids

by

Timothy Michael Winkler

A thesis submitted to the graduate faculty

in partial fulfillment of the requirements for the degree of

MASTER OF SCIENCE

Major: Aerospace Engineering

Program of Study Committee:

Bong Wie, Major Professor

Ran Dai

Vinay Dayal

Iowa State University

Ames, Iowa

2013

TABLE OF CONTENTS

LIST OF TABLES

LIST OF FIGURES

ACKNOWLEDGEMENTS

This research work has been supported in part by a NASA Innovative Advanced Concepts (NIAC) Phase 1 and 2 grants and by the Iowa Space Grant Consortium. I would like to thank Dr. John (Jay) Falker, the NIAC Program Executive, for his support. I would also like to thank my advisor, Dr. Bong Wie, for his support and guidance throughout this work, and for always pushing me to continuously improve and excel in my work.

ABSTRACT

Unmanned probes are the primary technologies used when exploring celestial bodies in our solar system. As these deep space exploration missions are becoming more and more complex, there is a need for advanced autonomous operation capabilities in order to meet mission objectives. These autonomous capabilities are required as ground-based guidance and navigation commands will not be able to be issued in real time due to the large distance from the Earth. For long-duration asteroid exploration missions, this also entails how to keep the spacecraft around or on the body in order for the mission to be successfully completed. Unlike with larger bodies such as planets, though, the dynamical environment around these smaller bodies can be difficult to characterize. The weak gravitational fields are not uniform due to irregular shapes and non-homogeneous mass distribution, especially when orbiting in close-proximity to the body. On top of that, small perturbation forces such as solar radiation pressure can be strong enough to destabilize an orbit around an asteroid.

The best solution for keeping a spacecraft in orbit about a small body is to implement some form of control technique. With conventional propulsion thrusters, active control algorithms tend to have a higher than acceptable propellant requirements for long-duration asteroid exploration missions, which has led to much research being devoted to finding open-loop solutions to long-term stable orbits about small bodies. These solutions can prove to be highly sensitive to the orbit's initial conditions, making them potentially unreliable in the presence of orbit injection errors. This research investigates a fuel-efficient, active control scheme to safely control a spacecraft's orbit in close-proximity to an asteroid. First, three different gravitational models capable of simulating the non-homogeneous gravity fields of asteroids are presented: the polyhedron gravity shape model, a spherical harmonics expansion, and an inertia dyadic gravity model. Then a simple feedback controller augmented by a disturbance-accommodating filter is employed to ensure orbital stability. Using these models and controller, several orbiting

cases as well as body-frame hovering are investigated to test the viability and fuel-efficiency of the proposed control system. The ultimate goal is to design an active orbit control system with minimum ΔV expenditure.

CHAPTER 1. INTRODUCTION

1.1 Motivation

Unmanned, robotic probes are the main tools at our disposal for studying celestial bodies such as asteroids, comets, and planets in our solar system. Of particular interest is to use these probes to explore the smaller, lesser known bodies such as asteroids or comets. Scientific interest in these objects focuses mainly on what they can tell us about the evolution and diversity of our solar system. As deep space exploration missions to these bodies become increasingly complex, spacecraft will require greater autonomous capabilities for systems such as guidance, navigation, and control as commands cannot be issued in real time. This is due to the need to first generate the proper commands on the ground based on measurements sent back by the spacecraft and then sent to the spacecraft from Earth causing a significant time delay between measurements and control commands. A primary concern for long-duration exploration missions operating in close-proximity to small bodies is how to reliably ensure the spacecraft remains in orbit around the body because many of the perturbing forces such as irregular gravitational fields are generally not well known in advance. On the other hand, enabling such a mission would require a thorough understanding of the dynamical environment around such a small body, or at the very least a control system capable of handling perturbing forces.

In the environment around an asteroid, relevant perturbation forces include the small, non-uniform gravitational field caused by a non-homogeneous mass distribution or irregular shape, solar radiation pressure, third-body gravitational effects, etc. For close-proximity operations, this results in highly perturbed, non-Keplerian orbits, which are difficult to characterize and predict [1]. It has also been shown by Scheeres [2], that the individual or combined effects of these forces can cause enough velocity change destabilize orbits, and cause the spacecraft to

impact of escape the asteroid.

The best solution to prevent something like this from occurring would be to implement some form of orbit control technique. In the case of the NEAR Shoemaker mission, one of the first missions to orbit an asteroid, near-continuous contact was maintained with the spacecraft with orbital correction maneuvers (OCMs) being designed and uploaded on a daily basis with careful consideration given to the orbit's stability [1, 3, 4]. While successful, this approach is very "hands on", and the spacecraft cannot react to unforeseen circumstances on its own. Large blocks of time were also required each day to download navigation measurements from the spacecraft, and then to upload ground-based navigation commands. More recently, NASA's Dawn spacecraft, which recently orbited the minor planet Vesta in 2011-2012 and is now en route to Ceres, handled orbital operations in a very similar manner with optical navigation data being downloaded to Earth daily [5]. The lowest orbit used in this mission around Vesta, though, was only 450 km in radius to avoid potential impact, which decreases the resolution of the camera images. Another proposed control solution was to hover above the body as was done in the JAXA Hayabusa mission to Itokawa [6, 7]. Hovering above a fixed-point above the asteroid is generally only appealing, from a scientific view, if it was desired to land on a particular part of the body. The propellant requirements for hovering and most forms of active control also tend to be substantially high, which could lead to shorter mission durations and a limited scientific return.

In an effort to avoid the requirements of active control, there has been much research devoted to finding open-loop solutions of orbits about small bodies and their stability bounds [2, 8–15]. While it is possible to find orbits that remain stable for great lengths of time, Figure 1.1 shows how three different orbits with similar initial conditions, affected only by the irregular gravitational field of the asteroid 433 Eros, can produce radically different results. The first orbit begins at a radius of 32.9 km along the positive inertial X-axis with a velocity equal to that of the local 2-body circular velocity. After numerically simulating the orbit for over a week, the orbit remains stable about the body. The second orbit has a radius of 32.8 km also at the local circular velocity, but is shifted 45° from the X-axis. Here the orbit remains about the body for over a week before finally escaping. The third orbit begins at a radius of 27.85

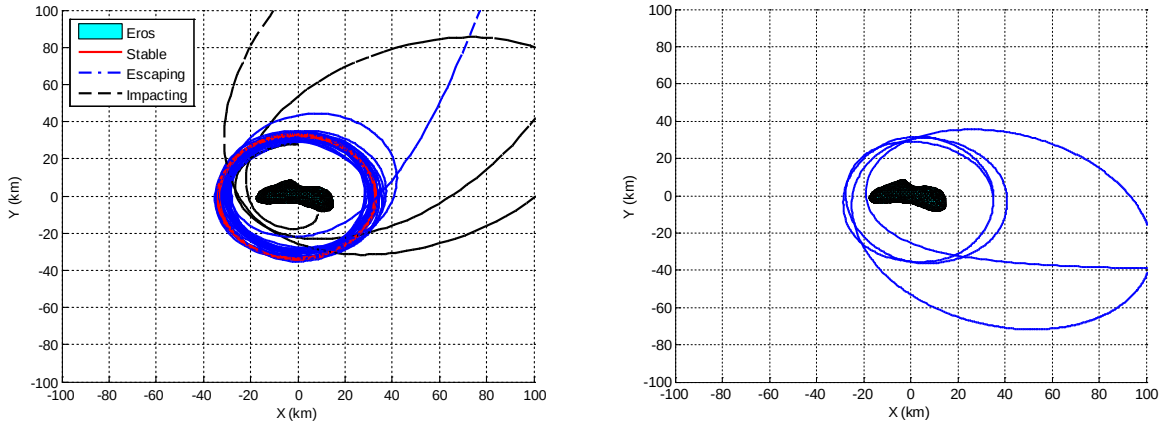

(a) Comparisons of stable, escaping, and impacting orbits around 433 Eros.

(b) Stable orbit with 5 percent velocity injection error.

Figure 1.1 Various orbits around 433 Eros. The coordinate system is an inertial frame fixed at Eros' center of mass with the positive Z-axis along the north pole spin axis. Eros is shown at initial conditions.

km along the inertial Y-axis with the local circular velocity. The orbit first travels far away from the body twice before impacting. Even though stable orbits can be found, Figure 1.1 also shows how an orbit injection error of 5 percent in the velocity is enough to destabilize the previous stable orbit, and cause the spacecraft to escape the body. Given the sensitivity of the dynamic environment at asteroids and comets to initial conditions, it is not practical to rely entirely upon open-loop solutions to keep a spacecraft in orbit about such a body.

1.2 Objectives and Organization

This research proposes a closed-loop alternative to open-loop orbiting with relatively small ΔV requirements. Such control capabilities would be invaluable in the areas of asteroid exploration as less time would have to be spent ensuring orbital stability on the ground, and could be devoted to the mission's scientific objectives instead. First, Chapter 2 will define the relevant coordinate system frames, and describe the equations of motion for an orbiting body. Next three different gravity models will be presented: the polyhedron shape model derived by Werner and Scheeres [16], the classical spherical harmonic expansion [17], and an inertia dyadic gravity model [18, 19]. Chapter 3 presents the control algorithms and the method for

reducing ΔV. The results are then presented in Chapter 4 followed by the conclusions and recommendations for further work in Chapter 5.

CHAPTER 2. DYNAMIC ENVIRONMENT MODELING

2.1 Coordinate Systems

Three separate coordinate systems are utilized in this work: a body-fixed frame (x, y, z), an inertial frame (X, Y, Z), and a spherical system $(r,\ \phi,\ \lambda)$. For the rest of this paper, lower case letters will denote quantities in the body-fixed frame and uppercase in the inertial frame. Each of these systems share their origins at the center of mass, and have the same z-axis, about which it is assumed the asteroid spins with a constant rotation rate ω. The body-fixed frame is used for integration of the equations of motion as well as hovering cases. The system aligns the x-, y-, and z-axes along the axes of minimum, intermediate, and maximum inertia respectively. The inertial frame shares its origin with the body-fixed frame, and is co-aligned with the body-fixed frame at the start of each simulation. Lastly, the spherical coordinate system measures a positive longitude angle (λ) from the body-fixed x-axis and a positive latitude angle (ϕ) from the xy-plane. Generally only the body-fixed and inertia frame will be used except when using the spherical harmonic gravity model. These systems are illustrated in Figures 2.1-2.2.

2.2 Dynamic Equation

For orbiting and proximity operations around an asteroid where the only perturbing force is gravity, the acceleration of the spacecraft in the body-fixed frame is

$$\ddot{\vec{r}} = \ddot{\vec{r}}|_B + 2\vec{\omega} \times \dot{\vec{r}}|_B + \vec{\omega} \times (\vec{\omega} \times \vec{r}) = \vec{g} + \vec{u} \tag{2.1}$$

where $\vec{r}$ is the spacecraft's position vector, $\dot{\vec{r}}|_B$ is the time derivative of $\vec{r}$ in the body-fixed frame, $\ddot{\vec{r}}|_B$ is the second time derivative of $\vec{r}$ in the body-fixed frame, $\vec{g}$ is the gravitational acceleration, $\vec{\omega}$ is the angular velocity vector of the asteroid, and $\vec{u}$ is the applied control

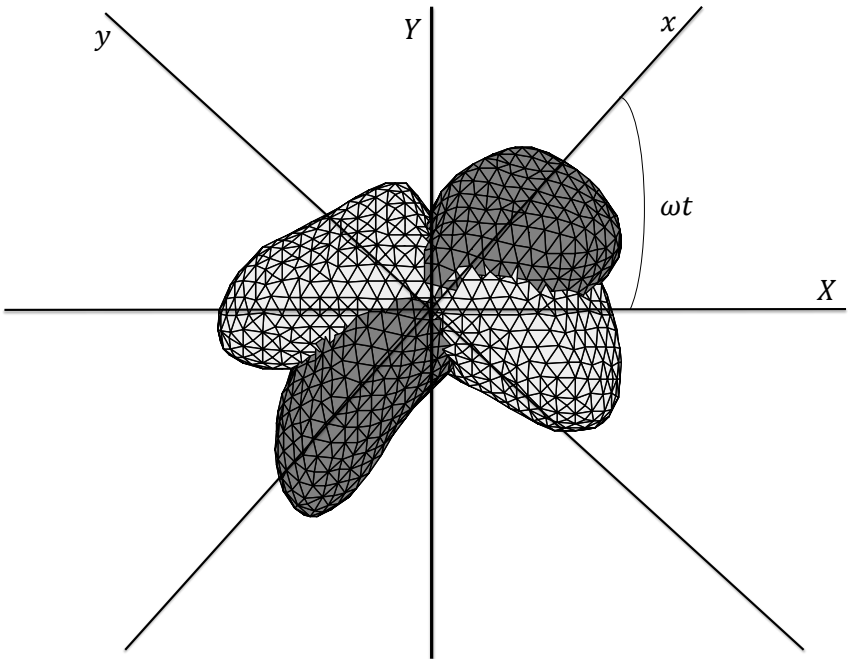

Figure 2.1 Inertial and body-fixed frame relation.

accelerations. Since it is assumed the asteroid has a uniform angular velocity about the z-axis, no $\dot{\vec{\omega}}$ term is included in Equation (2.1).

In the inertial frame, the dynamical equation is more simply expressed as

$$\ddot{\vec{r}} = \vec{g} + \vec{u} \tag{2.2}$$

As the body-fixed frame is uniformly rotating about the z-axis, these two frames are related by

$$\begin{bmatrix} X \\ Y \\ Z \end{bmatrix} = \begin{bmatrix} \cos(\omega t) & -\sin(\omega t) & 0 \\ \sin(\omega t) & \cos(\omega t) & 0 \\ 0 & 0 & 1 \end{bmatrix} \begin{bmatrix} x \\ y \\ z \end{bmatrix} \tag{2.3}$$

2.3 Spherical Harmonics Expansion

A classical approach to gravity modeling is to use a spherical harmonics expansion. Although reliable for modeling gravity during orbiting missions with the proper coefficients, the equations are only valid outside of the minimum circumscribing sphere around the body. The potential function in spherical harmonics is expressed as a double summation involving the

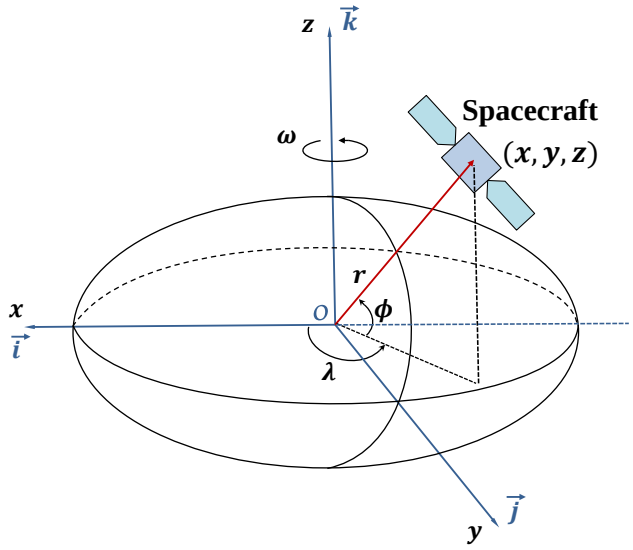

Figure 2.2 Spherical coordinate system with respect to the body-fixed frame.

associated Legendre polynomials, $P_{n,m}$, and the harmonic coefficients, $C_{n,m}$ and $S_{n,m}$ [17], as follows:

$$U = \frac{\mu}{r}\sum_{n=0}^{\infty}\sum_{m=0}^{n}\left(\frac{R}{r}\right)^n P_{n,m}[\sin(\phi)]\{C_{n,m}\cos(m\lambda) + S_{n,m}\sin(m\lambda)\} \tag{2.4}$$

$$P_{n,m}[\sin(\phi)] = \frac{1}{2^n n!}(1-\sin^2(\phi))^{m/2}\frac{d^{n+m}}{d\sin(\phi)^{n+m}}(\sin^2(\phi)-1)^n \tag{2.5}$$

where μ is the gravitational parameter, R is the reference radius of the circumscribing sphere, ϕ is the latitude, and λ is the longitude. It should be noted that all $S_{n,0}$ equal zero, and $C_{0,0}$ is one so that a zeroeth order expansion is the same as simple two body orbital motion. Should the coordinate system have its origin at the attracting body's center of mass, the coefficients $C_{1,0}$, $C_{1,1}$, and $S_{1,1}$ are all zero. In such a case, Equation (2.4) can be expressed as

$$U = \frac{\mu}{r}[1 + \sum_{n=2}^{\infty}\sum_{m=0}^{n}\left(\frac{R}{r}\right)^n P_{n,m}[\sin(\phi)]\{C_{n,m}\cos(m\lambda) + S_{n,m}\sin(m\lambda)\} \tag{2.6}$$

Here we will use the more general case given in Equation (2.4) to calculate the gradient of the potential in spherical coordinates before converting to a cartesian coordinate system to determine the gravitational acceleration vector, as follows:

$$\vec{g} = \frac{\partial U}{\partial r}\vec{e}_r + \frac{1}{r}\frac{\partial U}{\partial \phi}\vec{e}_\phi + \frac{1}{r\cos(\phi)}\frac{\partial U}{\partial \lambda}\vec{e}_\lambda \tag{2.7}$$

where

$$\frac{\partial U}{\partial r} = -\frac{\mu}{r^2}\sum_{n=0}^{\infty}\sum_{m=0}^{n}\left(\frac{R}{r}\right)^n (n+1)P_{n,m}[\sin(\phi)]\{C_{n,m}\cos(m\lambda) + S_{n,m}\sin(m\lambda)\} \quad (2.8a)$$

$$\frac{\partial U}{\partial \phi} = \frac{\mu}{r}\sum_{n=0}^{\infty}\sum_{m=0}^{n}\left(\frac{R}{r}\right)^n \{P_{n,m+1}[\sin(\phi)] - m\tan(\phi)P_{n,m}[\sin(\phi)]\}\{C_{n,m}\cos(m\lambda) + S_{n,m}\sin(m\lambda)\} \quad (2.8b)$$

$$\frac{\partial U}{\partial \lambda} = \frac{\mu}{r}\sum_{n=0}^{\infty}\sum_{m=0}^{n}\left(\frac{R}{r}\right)^n mP_{n,m}[\sin(\phi)]\{S_{n,m}\cos(m\lambda) - C_{n,m}\sin m\lambda\} \quad (2.8c)$$

The gravitational acceleration vector can then be converted from spherical coordinates to the body-fixed frame using the following transformation matrix

$$\mathbf{T} = \begin{bmatrix} \cos(\phi)\cos(\lambda) & -\sin(\phi)\cos(\lambda) & -\sin(\lambda) \\ \cos(\phi)\sin(\lambda) & -\sin(\phi)\sin(\lambda) & \cos(\lambda) \\ \sin(\phi) & \cos(\phi) & 0 \end{bmatrix} \quad (2.9)$$

The derivation above assumes the case when the harmonic coefficients are not normalized. Often the coefficients will be given as normalized values to avoid numerical difficulties associated with of the gravitational coefficients becoming very small as the degree and order get large. In some computers, this would introduce truncation errors so normalization becomes necessary to prevent inaccuracy. One method of normalization used in this work is

$$\prod_{n,m} = \sqrt{\frac{(n+m)!}{(n-m)!k(2n+1)}} \quad (2.10)$$

$$k = 1 \quad if \quad m = 0$$

$$k = 2 \quad if \quad m \neq 0$$

$$\bar{S}_{n,m} = \prod_{n,m} S_{n,m} \qquad \bar{C}_{n,m} = \prod_{n,m} C_{n,m} \qquad \bar{P}_{n,m} = \frac{P_{n,m}}{\prod_{n,m}} \quad (2.11)$$

It is important to remember to normalize the Legendre polynomials as well when using normalized coefficients because their product must remain the same (i.e. $\bar{C}_{n,m}\bar{P}_{n,m} = C_{n,m}P_{n,m}$ and $\bar{S}_{n,m}\bar{P}_{n,m} = S_{n,m}P_{n,m}$)

2.4 Polyhedron Shape Model

The polyhedron gravitational model can be advantageous when the gravitating body has a complex, irregular shape. Although computationally slower than using a spherical harmonics

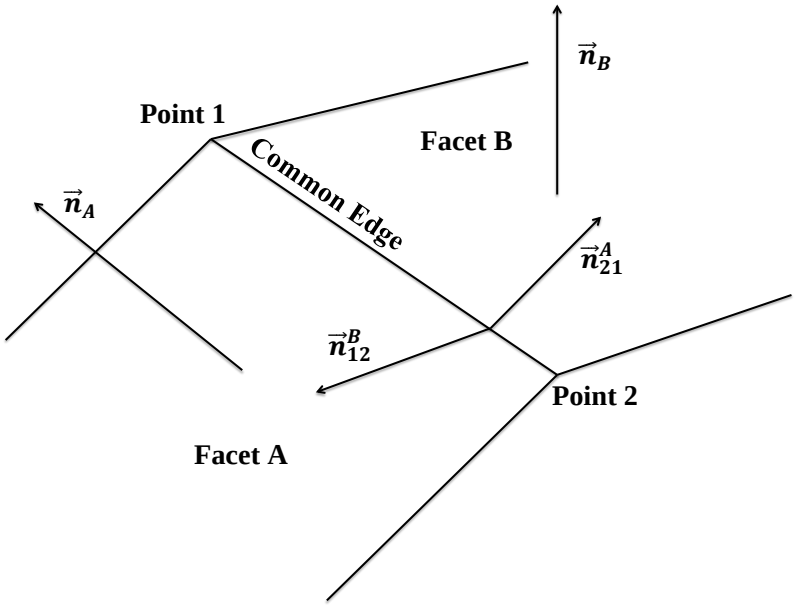

Figure 2.3 Illustration of the unit facet normal and unit edge normal vectors.

expansion, the model is valid anywhere around the body, whereas the spherical harmonics expansion is only valid outside of a circumscribing sphere. Here we will show the equations used to simulate the gravitational attraction of a polyhedron model. Note that these equations assume a constant density, and that the shape model uses triangular facets. The complete derivation is given by Werner and Scheeres in [16]. We will start with the potential function described as

$$U = \frac{1}{2}G\rho \sum_{e \in edges} L_e \vec{r}_e \cdot \widetilde{E}_e \cdot \vec{r}_e - \frac{1}{2}G\rho \sum_{f \in facets} \omega_f \vec{r}_f \cdot \widetilde{F}_f \cdot \vec{r}_f \tag{2.12}$$

where G is the gravitational constant, ρ is the density, $\vec{r}_e$ is a vector from a point in space to an edge on the polyhedron model and $\vec{r}_f$ to a facet, $\widetilde{E}_e$ is an edge dyad, L_e is a dimensionless per-edge factor, $\widetilde{F}_f$ is a facet dyad, and ω_f is a dimensionless per-facet factor. $\widetilde{E}_e$ and $\widetilde{F}_f$ are given by

$$\widetilde{E}_e = \vec{n}_A \vec{n}_{21}^A + \vec{n}_B \vec{n}_{12}^B \tag{2.13}$$

$$\widetilde{F}_f = \vec{n}_f \vec{n}_f \tag{2.14}$$

where $\vec{n}_f$, $\vec{n}_A$, and $\vec{n}_B$ are outward-facing unit normal vectors and $\vec{n}_{21}^A$ and $\vec{n}_{12}^B$ are outward-facing edge unit normal vectors. A graphical illustration of these unit vectors is shown in

Figure 2.3. For a coordinate system, whose origin lies within the polyhedron, the outward-facing facet normal vectors can be calculated using

$$\vec{n}_f = (\vec{r}_2 - \vec{r}_1) \times (\vec{r}_3 - \vec{r}_2) = \vec{r}_1 \times \vec{r}_2 + \vec{r}_2 \times \vec{r}_3 + \vec{r}_3 \times \vec{r}_1 \tag{2.15}$$

where $\vec{r}_1$, $\vec{r}_2$, and $\vec{r}_3$ are vectors from the origin to each of the three vertices that define the triangular facet, and $\vec{n}_f$ is the facet normal vector. In computer modeling applications, the vertices that define each facet are stored in a matrix using either a clockwise or counterclockwise rotation. The rotation direction refers to the direction around the facet you would have to travel to find next vertex point. Equation (2.15) assumes a counterclockwise rotation. For clockwise rotation storage, simply multiply the equation by -1. If the storage method is unknown, this can also be checked by taking the dot product between $\vec{n}_f$ and one of the vertex vectors. A positive product indicates the vector is outward-facing. The outward facing edge normal vectors, also assuming a counterclockwise rotation, are

$$\vec{n}_{12}^{f} = (\vec{r}_2 - \vec{r}_1) \times \vec{n}_f \tag{2.16a}$$

$$\vec{n}_{23}^{f} = (\vec{r}_3 - \vec{r}_2) \times \vec{n}_f \tag{2.16b}$$

$$\vec{n}_{31}^{f} = (\vec{r}_1 - \vec{r}_3) \times \vec{n}_f \tag{2.16c}$$

Next the dimensionless factors L_e and ω_f are given as

$$L_e = \ln \frac{r_i + r_j + e_{ij}}{r_i + r_j - e_{ij}} \tag{2.17}$$

$$\omega_f = 2 \arctan \frac{\vec{r}_i \cdot \vec{r}_j \times \vec{r}_k}{r_i r_j r_k + r_i(\vec{r}_j \cdot \vec{r}_k) + r_j(\vec{r}_k \cdot \vec{r}_i) + r_k(\vec{r}_i \cdot \vec{r}_j)} \tag{2.18}$$

where $\vec{r}_i$, $\vec{r}_j$, and $\vec{r}_k$ are vectors from the field point to one of the three vertices on the triangular facet, r_i,r_j, and r_k are the magnitudes of the vectors, and e_{ij} is the length of the edge connecting $\vec{r}_i$ and $\vec{r}_j$. Note that per facet, there will be one value of ω_f and three for L_e (one for each edge). The gradient of the potential in Equation (2.12) is expressed as

$$\nabla U = -G\rho \sum_{e \in edges} L_e \widetilde{E}_e \cdot \vec{r}_e + G\rho \sum_{f \in facets} \omega_f \widetilde{F}_f \cdot \vec{r}_f \tag{2.19}$$

The model also has a simple method for determining whether or not a field point is outside of the polyhedron by evaluating the Laplacian of the potential

$$\nabla^2 U = -G\rho \sum_{f \in facets} \omega_f \tag{2.20}$$

The sum of ω_f goes to zero when the field point is located outside of the polyhedron, and 4π inside the polyhedron. This is particularly helpful in knowing during a simulation whether or not a spacecraft remained in orbit about a body, or crashed into the surface without requiring much additional computation as ω_f is already required in Equation (2.19). Equation (2.20), however, will not provide any information if the spacecraft escaped the gravitational field of the body. This can only be determined by analyzing the results after a simulation.

2.5 Inertia Dyadic Gravity Model

The third and final model is the inertia dyadic gravitational model as described in [18] and [19]. For a continuous body with density ρ, the gravitational attraction on a point with mass m can be expressed as

$$\vec{F} = -Gm \int \vec{p}(\vec{p} \cdot \vec{p})^{-3/2} \rho dV \tag{2.21}$$

where $\vec{p}$ is the position vector of a point mass m with respect to the body. If $\vec{p}$ is replaced by a vector addition from a point in the body to its center of mass and then to the point mass as shown in Figure 2.4, the gravitational force is found to be

$$\vec{F} = -\frac{G\bar{m}m}{R^2}[\vec{e}_r + \sum_{i=2}^{\infty} \vec{f}^{(i)}] \tag{2.22}$$

where $\bar{m}$ is the mass of the attracting body, R is the distance to the center of mass, $\vec{e}_r$ is a unit vector along $\vec{R}$, and $\vec{f}^{(i)}$ is a collection of terms of the ith degree in $|\vec{r}|/R$. For example, the term $\vec{f}^{(2)}$ is given by

$$\vec{f}^{(2)} = \frac{1}{mR^2}\{\frac{3}{2}[tr(\widetilde{I}) - 5\vec{e}_r \cdot \widetilde{I} \cdot \vec{e}_r]\vec{e}_r + 3\widetilde{I} \cdot \vec{e}_r\} \tag{2.23}$$

where $\widetilde{I}$ is the inertia dyadic of the gravitating body and $tr(\widetilde{I})$ is defined as

$$tr(\widetilde{I}) = \vec{e}_1 \cdot \widetilde{I} \cdot \vec{e}_1 + \vec{e}_2 \cdot \widetilde{I} \cdot \vec{e}_2 + \vec{e}_3 \cdot \widetilde{I} \cdot \vec{e}_3 \tag{2.24}$$

where $\vec{e}_1$, $\vec{e}_2$, and $\vec{e}_3$ are unit vectors in the appropriate, orthogonal coordinate system. Since $\widetilde{I}$ in matrix form is given as

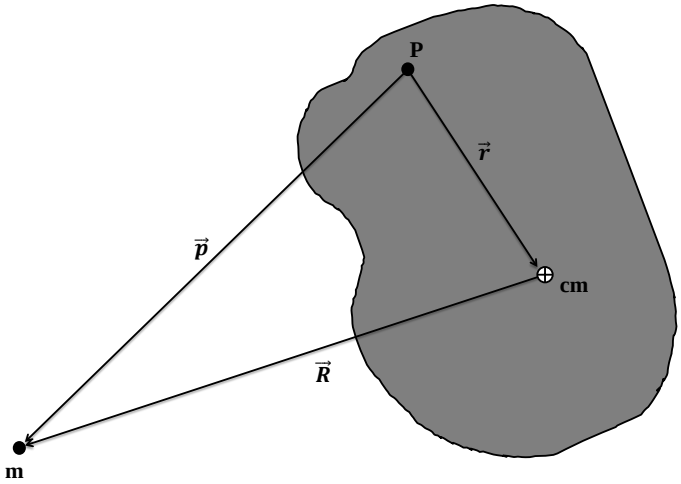

Figure 2.4 Illustration of vectors in the inertia dyadic gravity model.

$$\widetilde{I} = \begin{bmatrix} \vec{e}_1 & \vec{e}_2 & \vec{e}_3 \end{bmatrix} \begin{bmatrix} I_{11} & I_{12} & I_{13} \\ I_{21} & I_{22} & I_{23} \\ I_{31} & I_{32} & I_{33} \end{bmatrix} \begin{bmatrix} \vec{e}_1 \\ \vec{e}_2 \\ \vec{e}_3 \end{bmatrix} \tag{2.25}$$

Equation (2.24) simplifies to

$$tr(\widetilde{I}) = I_{11} + I_{22} + I_{33} \tag{2.26}$$

According to Equation (2.26), Equation (2.24) can be thought of being similar to the trace operation for matrices, which sums the diagonal components of a matrix. If the coordinate system is aligned with the principal axes of the body, Equation 2.26 sums the principal moments of inertia (i.e. $I_{xx}+I_{yy}+I_{zz}$). When the inertia dyadic is given in the principal coordinate system instead of in spherical coordinates, the $\vec{f}^{(2)}$ term must be expressed in the body-fixed frame instead of spherical coordinates. Using the transformation matrix from spherical coordinates to the body-fixed frame in Equation 2.9, the unit vector $\vec{e}_r$ can be substituted with

$$\vec{e}_r = (\cos(\phi)\cos(\lambda))\vec{e}_x + (\cos(\phi)\sin(\lambda))\vec{e}_y + \sin(\phi)\vec{e}_z \tag{2.27}$$

This research will only use the $\vec{f}^{(2)}$ term when calculating the gravitational force as the higher moments of inertia have generally not been evaluated and made publicly available for

asteroids and other small bodies. If desired, higher order terms can be included for increased accuracy, which are expressed in terms of the higher moments of inertia [19].

2.6 Gravity Model Comparisons

When simulating an asteroid's gravity, the polyhedron shape model requires noticeably more computation time than either the spherical harmonic expansion or the inertia dyadic models. This comes from the fact that the polyhedron model sums contributions from each facet and facet edge. Reasonably accurate models will include at least several thousand facets as opposed to a 15^{th} order harmonic expansion, which sums 136 elements, or the moment-of-inertia model, which sums elements equal to the order.

These gravity models are applied to the large, near-Earth asteroid 433 Eros. This asteroid has measured center of mass is very close to the center of mass assuming a uniform internal structure [20, 21]. This results in a near constant density, which is required for the polyhedron gravity model. Eros is also a prime example of an asteroid with a very irregular shape with the largest dimension being more than twice as long as the smallest dimension. Figure 2.5 plots the strength of the gravitational field around the large, near-Earth asteroid 433 Eros using these three models and basic 2-body, point mass gravity. As the magnitude of the gravitational force is rather weak, the log of this force is used for graphical illustration. Away from the surface of the body, both the polyhedron shape model and the harmonic expansion exhibit almost identical results with the inertia dyadic model having the same trend but slightly different magnitudes. Nearer to the surface, the inertia dyadic model starts to exhibit a relatively strong gravitational field as opposed to the polyhedron shape model. This difference with the inertia dyadic model is likely due to the low order used to calculate the gravitational force (only the $\vec{f}^{(2)}$ term was included). Of note as well is that the further away from the gravitating body, the more closer each model becomes to a simple point mass approximation. For orbits closer to the body, the non-uniform effects are more apparent, and diverge from the point mass approximation. Figure 2.6 then focuses on the surface gravitational acceleration computed from the polyhedron shape model. Consistent with the gravity field from Figure 2.5, the gravitational force is relatively strong in the middle of the shape and decreases towards the far ends.

Table 2.1 Characteristics of 433 Eros [20, 22].

Physical Properties	Values		
semi x-axis, y-axis, z-axis	16.7 km	8.6 km	6.3 km
bulk density		2.67 g/cm^3	
GM		4.463e-4 km^3/s^2	
rotation period		5.27 hours	
J_2, J_3	0.0525	0.0014	
Inertia Matrix			
I_{xx}, I_{xy}, I_{xz}	1.117e23 kg·m^2	6.232e22 kg·m^2	-2.257e20 kg·m^2
I_{yx}, I_{yy}, I_{yz}	6.232e22 kg·m^2	4.793e23 kg·m^2	-2.589e19 kg·m^2
I_{zx}, I_{zy}, I_{zz}	-2.257e20 kg·m^2	-2.589e19 kg·m^2	4.978e23 kg·m^2
Normalized Inertia Matrix			
I_{xx}, I_{xy}, I_{xz}	16.709 km^2	9.319 km^2	-0.034 km^2
I_{yx}, I_{yy}, I_{yz}	9.319 km^2	71.669 km^2	-0.004 km^2
I_{zx}, I_{zy}, I_{zz}	-0.034 km^2	-0.004 km^2	74.443 km^2

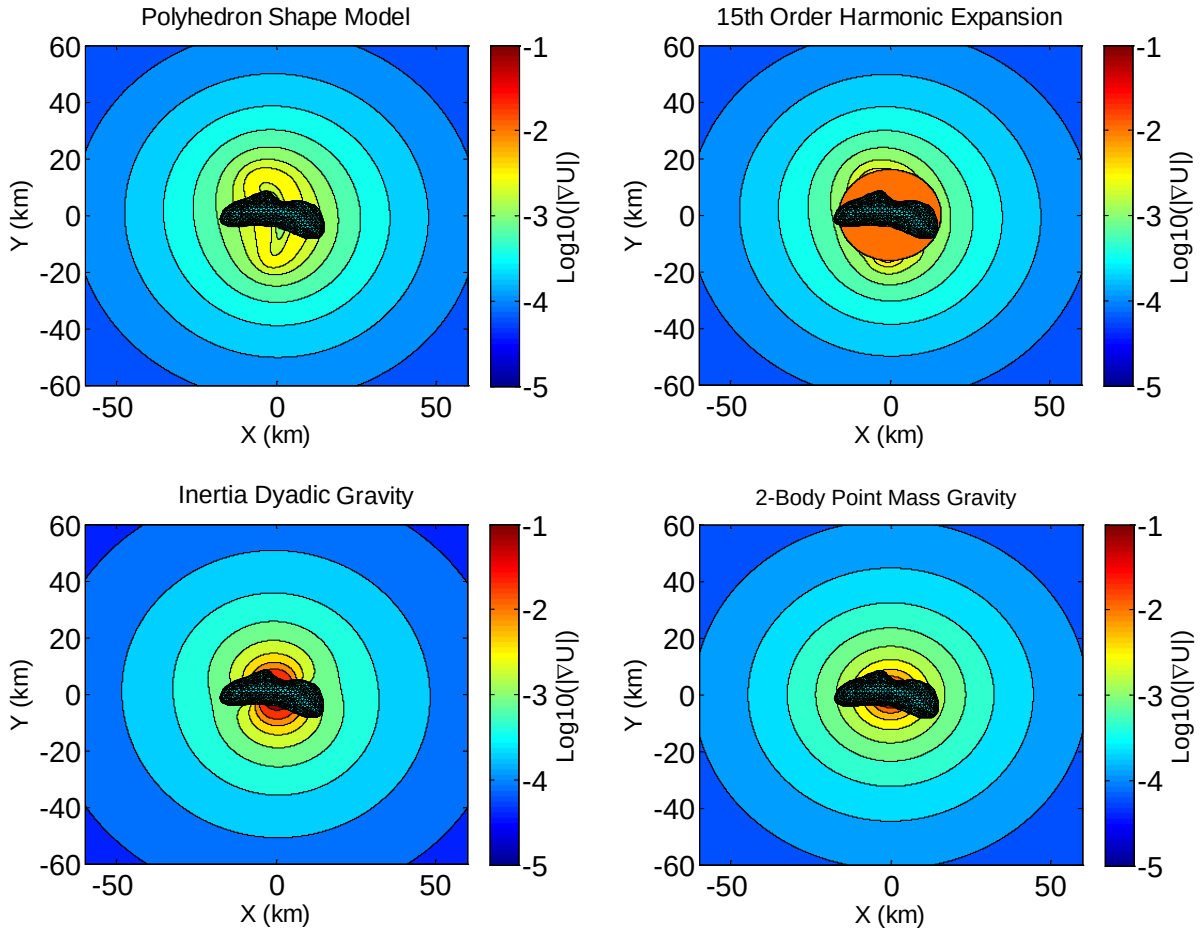

Figure 2.5 Gravitational field comparisons of the three gravitational models.

(a) 3D model of 433 Eros based on NEAR's Laser Rangefinder measurements.

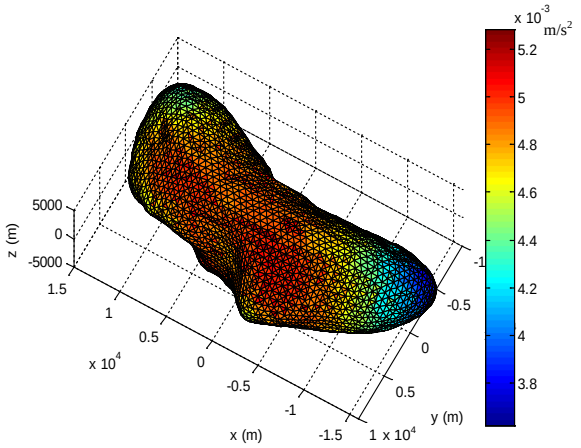

(b) Surface gravitational acceleration from the polyhedron shape model.

Figure 2.6 Image of 433 Eros derived from the NEAR Shoemaker measurements shown next to the plate model used for the polyhedron gravity model.

CHAPTER 3. STATE-FEEDBACK CONTROL

3.1 PD Control

Proportional-derivative (PD) control is a subset of the more general full-state feedback control, a simple, common form of feedback control logic. This type of control attempts to minimize the error between measured variables and their reference values by feeding back the error multiplied by some controller gain as the control input. With PD control, the integral control gains are set to zero leaving only the proportional and derivative gains. To implement this control, the equations of motion will first be expressed in state-space form. As the gravitational terms are highly nonlinear, they are included only as external disturbances ($\mathbf{w}$) to give a simple dynamical model as

$$\dot{\mathbf{x}}_p = \mathbf{A}_p\mathbf{x}_p + \mathbf{B}_p\mathbf{u} + \mathbf{w} \tag{3.1}$$

$$\mathbf{x}_p = \begin{bmatrix} X \\ Y \\ Z \\ \dot{X} \\ \dot{Y} \\ \dot{Z} \end{bmatrix}, \quad \mathbf{u} = \begin{bmatrix} u_x \\ u_y \\ u_z \end{bmatrix}, \quad \mathbf{A}_p = \begin{bmatrix} 0 & 0 & 0 & 1 & 0 & 0 \\ 0 & 0 & 0 & 0 & 1 & 0 \\ 0 & 0 & 0 & 0 & 0 & 1 \\ 0 & 0 & 0 & 0 & 0 & 0 \\ 0 & 0 & 0 & 0 & 0 & 0 \\ 0 & 0 & 0 & 0 & 0 & 0 \end{bmatrix}, \quad \mathbf{B}_p = \begin{bmatrix} 0 & 0 & 0 \\ 0 & 0 & 0 \\ 0 & 0 & 0 \\ 1 & 0 & 0 \\ 0 & 1 & 0 \\ 0 & 0 & 1 \end{bmatrix}, \quad \mathbf{w} = \begin{bmatrix} 0 \\ 0 \\ 0 \\ w_x \\ w_y \\ w_z \end{bmatrix}$$

The control input ($\mathbf{u}$) is defined to be

$$\mathbf{u} = -\mathbf{K}(\mathbf{x}_p - \mathbf{x}_r) \tag{3.2}$$

where $\mathbf{K}$ is the control gain matrix to be determined, and $\mathbf{x}_r$ are the reference variables. For an arbitrary, periodic orbit, these values are given by

$$X_r(t) = A_x \cos(\omega_x t) \tag{3.3a}$$

$$Y_r(t) = A_y \sin(\omega_y t) \tag{3.3b}$$

$$Z_r(t) = A_z \sin(\omega_z t) \tag{3.3c}$$

$$\dot{X}_r(t) = -A_x \omega_x \sin(\omega_x t) \tag{3.3d}$$

$$\dot{Y}_r(t) = A_y \omega_y \cos(\omega_y t) \tag{3.3e}$$

$$\dot{Z}_r(t) = A_z \omega_z \cos(\omega_z t) \tag{3.3f}$$

where A_x, A_y, and A_z are the amplitudes of the reference values along the X-, Y-, and Z-axes respectively and ω_x, ω_y, and ω_z are the frequencies. Substituting the control input into Equation (3.1) yields the new system

$$\dot{\mathbf{x}}_p = (\mathbf{A}_p - \mathbf{B}_p\mathbf{K})\mathbf{x}_p + \mathbf{K}\mathbf{x}_r + \mathbf{w} \tag{3.4}$$

3.2 Disturbance-Accommodating Control

Disturbance-accommodating or disturbance-rejection control is a technique which can be used to reduce the control effort in the presence of persistent disturbances [23, 24]. This control works by eliminating parts of the control acceleration, and allows the spacecraft to follow a trajectory that is closer to a natural periodic solution of the nonlinear equations of motion. As we are forcing the spacecraft to follow a particular reference orbit with PD control, the nonlinear gravitational effects can cause constant and/or periodic disturbances, which require a higher control magnitude to cancel out. As little to nothing is known about the gravitational fields of asteroids, these disturbances cannot be accurately modeled beforehand,. Therefore we use an iterative design method to construct a disturbance-accommodating controller. This method allows the spacecraft to deviate from the reference trajectory and follow one that requires less ΔV.

When first orbiting the gravitating body with only PD control, there exist certain frequency components (disturbances) in the controlled orbit that need to be consistently damped out via the control acceleration. These components can be found by examining an FFT (Fast Fourier

Transform) plot of the control commands along each axis. Once the spectral components have been identified, we can design periodic disturbance-accommodation filters of the form

$$\ddot{\alpha}_i + \omega_{xi}^2 \alpha_i = u_x \tag{3.5a}$$

$$\ddot{\beta}_i + \omega_{yi}^2 \beta_i = u_y \tag{3.5b}$$

$$\ddot{\gamma}_i + \omega_{zi}^2 \gamma_i = u_z \tag{3.5c}$$

where ω_{xi}, ω_{yi}, and ω_{zi} represent the ith frequency component in each axis, and α, β, and γ are the corresponding disturbed filter states. If the control inputs are sinusoidal, the solutions to these differential equations will also be sinusoidal. For constant disturbances, the filters take the form of

$$\dot{\alpha} = u_x \tag{3.6a}$$

$$\dot{\beta} = u_y \tag{3.6b}$$

$$\dot{\gamma} = u_z \tag{3.6c}$$

The disturbance-accommodation filter can include as many frequencies as are present in the FFT plots. The filter can then be described in state space form

$$\dot{\mathbf{x}}_d = \mathbf{A}_d \mathbf{x}_d + \mathbf{B}_d \mathbf{u} \tag{3.7}$$

$$\mathbf{x}_d = \begin{bmatrix} \alpha_i \\ \beta_i \\ \gamma_i \\ \dot{\alpha}_i \\ \dot{\beta}_i \\ \dot{\gamma}_i \end{bmatrix}, \quad \mathbf{A}_d = \begin{bmatrix} 0 & 0 & 0 & 1 & 0 & 0 \\ 0 & 0 & 0 & 0 & 1 & 0 \\ 0 & 0 & 0 & 0 & 0 & 1 \\ -\omega_{xi}^2 & 0 & 0 & 0 & 0 & 0 \\ 0 & -\omega_{yi}^2 & 0 & 0 & 0 & 0 \\ 0 & 0 & -\omega_{zi}^2 & 0 & 0 & 0 \end{bmatrix}, \quad \mathbf{B}_d = \begin{bmatrix} 0 & 0 & 0 \\ 0 & 0 & 0 \\ 0 & 0 & 0 \\ 1 & 0 & 0 \\ 0 & 1 & 0 \\ 0 & 0 & 1 \end{bmatrix}$$

where $\mathbf{x}_d$ is the disturbance filter state vector. It should be noted that if a frequency or bias component is not used during the iteration, the corresponding filter state is not included in $\mathbf{x}_d$. The disturbance filter in Equation (3.7) can then be augmented to the system in Equation (3.1) as follows:

$$\begin{bmatrix} \dot{\mathbf{x}}_p \\ \dot{\mathbf{x}}_d \end{bmatrix} = \begin{bmatrix} \mathbf{A}_p & 0 \\ 0 & \mathbf{A}_d \end{bmatrix} \begin{bmatrix} \mathbf{x}_p \\ \mathbf{x}_d \end{bmatrix} + \begin{bmatrix} \mathbf{B}_p \\ \mathbf{B}_d \end{bmatrix} \mathbf{u} \tag{3.8}$$

For a system described by Equation (3.8), with an augmented system matrix $\mathbf{A}$, the control is now expressed as

$$\mathbf{u} = -\mathbf{K} \begin{bmatrix} \mathbf{x}_p - \mathbf{x}_r \\ \mathbf{x}_d \end{bmatrix} \tag{3.9}$$

In an iterative design, spectral components are identified and added to the disturbance filter state in Equation (3.7) each time the control is updated. These iterations are necessary as suppressing frequency components in the control can potentially result in different frequency components appearing in the control. Normally these frequency components can be characterized as some integer combination of the body spin rate and the orbit frequency. After several iterations, a disturbance-accommodating controller can be designed that results in a drastic reduction of ΔV. All that is left is find the control gain matrix $\mathbf{K}$, which will be discussed further in the next section.

3.3 Linear Quadratic Regulator

One method to determine the control gain matrix $\mathbf{K}$ is the linear quadratic regulator (LQR) method. The LQR method uses optimal control theory to solve for a $\mathbf{K}$ to minimize the following performance index

$$J = \frac{1}{2} \int_0^\infty (\mathbf{x}^T \mathbf{Q} \mathbf{x} + \mathbf{u}^T \mathbf{R} \mathbf{u}) dt \tag{3.10}$$

where $\mathbf{Q}$ and $\mathbf{R}$ are user-chosen weighting matrices. Once selected, the control gain matrix $\mathbf{K}$ is found as [24]

$$\mathbf{K} = \mathbf{R}^{-1} \mathbf{B}^T \mathbf{X} \tag{3.11}$$

where $\mathbf{X}$ is the symmetric positive semidefinite solution of the algebraic Riccati equation (ARE)

$$\mathbf{A}^T \mathbf{X} + \mathbf{X} \mathbf{A} - \mathbf{X} \mathbf{B} \mathbf{R}^{-1} \mathbf{B}^T \mathbf{X} + \mathbf{Q} = 0 \tag{3.12}$$

For a unique solution of $\mathbf{X}$ to exist, four conditions must be met:

1. $\mathbf{Q}$ must be symmetric and positive semidefinite;

2. $\mathbf{R}$ must be symmetric and positive definite;

3. the pair $(\mathbf{A}, \mathbf{B})$ must be controllable (stabilizable);

4. the pair $(\mathbf{A}, \sqrt{\mathbf{Q}}^T \sqrt{\mathbf{Q}})$ must be observable (detectable).

3.3.1 Bryson Method

For the simpler case of pure PD control, the selection of $\mathbf{Q}$ and $\mathbf{R}$ is not very important as most viable matrix choices result in similar performance in terms of stability and ΔV expenditure. Once multiple disturbance-accommodating filters are added, though, the components of weighting matrices have a much greater influence on the system's performance. If improperly selected, the control will not necessarily be near optimum, and results in higher fuel consumption. It is possible to go about this selection process using a trial-and-error process as with PD control to obtain satisfactory results. The downside to this approach is that it requires a longer time to complete, especially when the system becomes very complex with a large number of disturbance filter states. An alternative method, which can provide a good starting point to reduce the number of design iterations, is the Bryson method [25–27]. This method first assumes that $\mathbf{Q}$ and $\mathbf{R}$ are diagonal matrices.

$$\mathbf{Q} = diag[q_1, ..., q_n], \qquad \mathbf{R} = diag[r_1, ..., r_m] \tag{3.13}$$

The diagonal elements of these matrices are given as

$$q_i = \frac{1}{x_i^2(max)}, \qquad i = 1, 2, ..., n \tag{3.14a}$$

$$r_j = \frac{1}{u_j^2(max)}, \qquad j = 1, 2, ..., m \tag{3.14b}$$

where $x_i(max)$ and $u_j(max)$ represent the anticipated maximum allowable values of the state variables and control inputs respectively. If this value is well known, then it will have to be estimated. Intuitively Equation 3.14 makes sense as variables with tight motion constraints will have a higher weighting for minimization, whereas variables that are allowed to vary largely are given less weight.

CHAPTER 4. SIMULATION AND RESULTS

The previously described gravity models and control techniques are once again applied the 433 Eros. First we will compare the inertia dyadic gravity model with only the $\vec{f}^{(2)}$ term against various orders of the spherical harmonics expansion. Then using only the polyhedron shape and spherical harmonics gravity models, we will examine five different orbiting scenarios: a prograde and retrograde orbit in the XY-plane, a 45° inclined orbit, a polar orbit, and hovering in the body-fixed reference frame. In each of these scenarios, the spacecraft will follow a 35 km radius circular reference orbit with PD control before disturbance-accommodating filters are added. Current missions do not typically follow orbits so close to an asteroid, but future missions are desired to orbit as close as possible to the body. Being able to orbit closer to the asteroid also allows scientists to observe the object in greater detail, and serves to demonstrate the capabilities of disturbance-accommodating filtering. For these simulations, it is assumed that all of the states can be measured for feedback control and the thrusters are capable of producing the required control accelerations. All scenarios assume an asteroid density of 2.67 g/cm^3 and rotation period of 5.27 hours, and the spherical harmonics uses a reference radius of 16 km. The shape model, spherical harmonic coefficients, and the inertia dyadic were downloaded from NASA's website of shape and gravity models produced by the NEAR Shoemaker mission [22].

4.1 Inertia Dyadic Gravity Model Results

Here a 35 km radius prograde orbit with PD control in the XY-plane is examined using the inertia dyadic gravity model, a 15^{th} order harmonics expansion, and a 2^{nd} order harmonics expansion. As can be seen in Figure 4.1, there is a slight magnitude difference in the X- and Y-directions between the 15^{th} order expansion and the other two models. There is a much larger

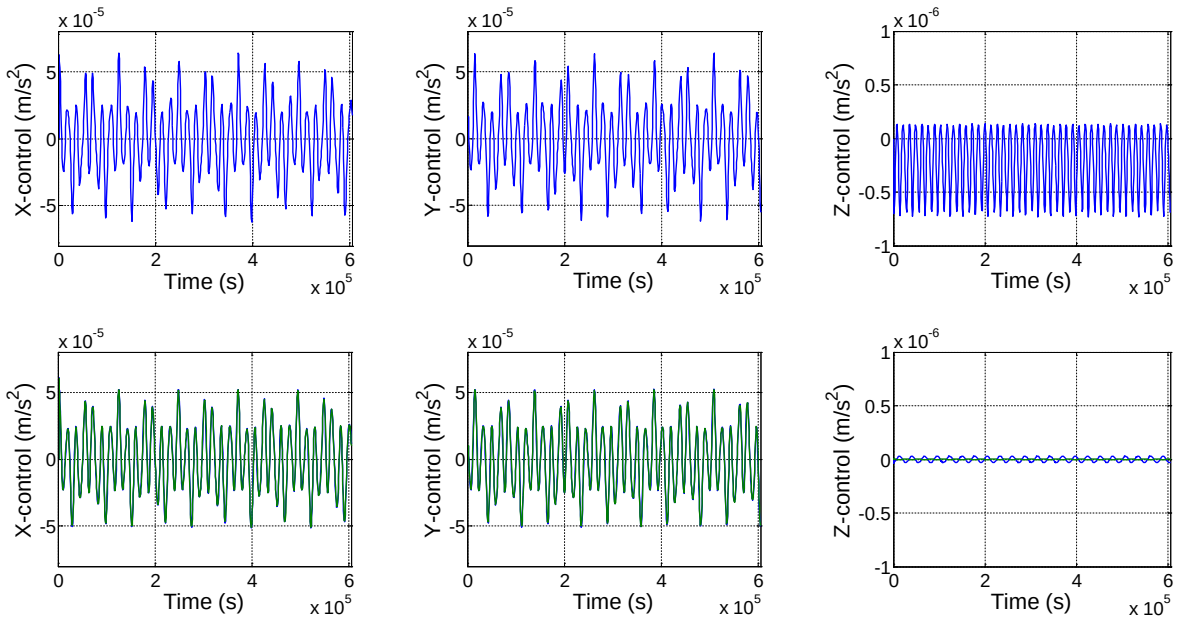

Figure 4.1 Control acceleration histories for the 15^{th} order expansion, 2^{nd} order expansion, and inertia dyadic models. The 15^{th} order model is plotted on the top and both the 2^{nd} order and inertia dyadic models are overlayed on the bottom.

distinction in the Z-direction for the given plotting scales, but as the control accelerations in this direction are an entire order of magnitude smaller than in the X- or Y-direction, these variations are hardly noticeable when computing the ΔV requirements. To illustrate this, the control accelerations can be integrated to give a ΔV result of 20.6 m/s for the inertia dyadic model, 21.37 m/s for the 15^{th} order expansions, and 20.42 m/s for the 2^{nd} order expansion, which are all within 1 m/s of each other. Similarly with the FFT plots in Figure 4.2, there is little difference between the three models in the X- and Y-direction, but a noticeable difference in the Z-direction. Here it is easier to notice that there is virtually no difference between the inertia dyadic model and a 2^{nd} order harmonic expansion. They are both capable of being utilized to find the three major frequencies present along the X- and Y-axes, but leave out the higher frequencies with small amplitudes noticeable with the higher order expansion. It is highly likely that including terms of a sufficiently high order in $\vec{f}^{(i)}$ would be capable of simulating these smaller frequency components.

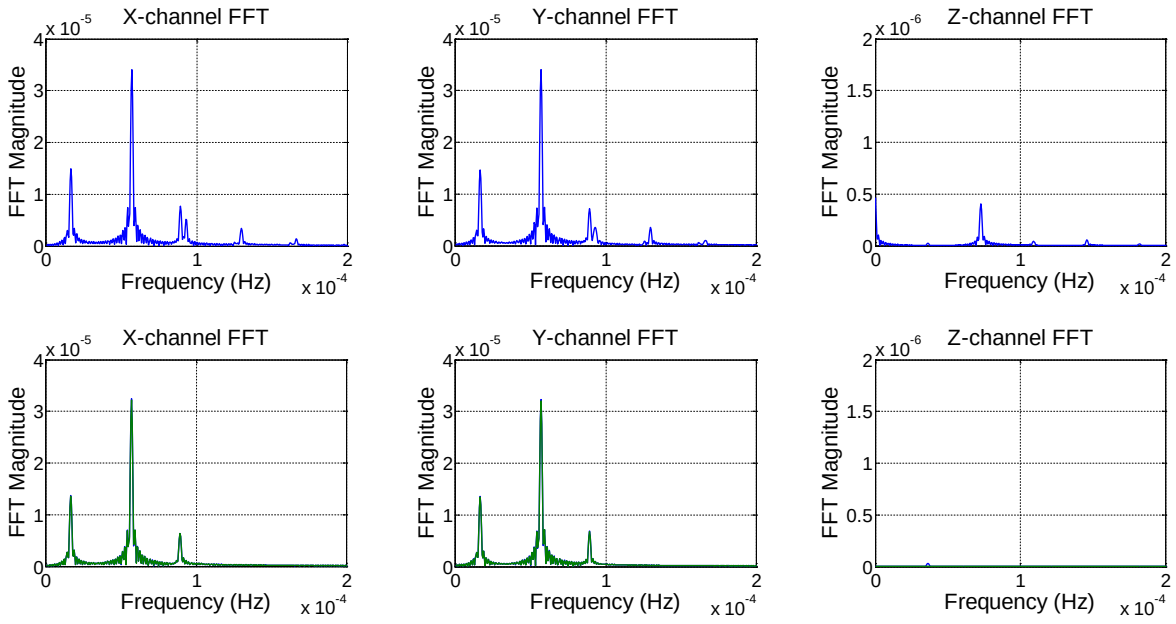

Figure 4.2 FFT plots for the 15^{th} order expansion, 2^{nd} order expansion, and inertia dyadic models. The 15^{th} order model is plotted on the top and both the 2^{nd} order and inertia dyadic models are overlayed on the bottom.

4.2 XY-Plane Prograde Orbit

Now we will examine a prograde orbit in the XY-plane about the asteroid. The orbit begins on the positive X-axis at the local circular velocity. The resulting orbits, control accelerations, and FFT plots with only PD control are given in Figures 4.3-4.5. In Figure 4.4, a quick comparison between the polyhedron model and the harmonics model results show very little difference in the X- and Y-control and a slight bias difference in the Z-control. Considering that the Z-control is two orders of magnitude smaller than the more prominent X- and Y-control, the Z-control difference is essentially negligible. Integrating these control accelerations results in a ΔV of 21.13 m/s per week with the polyhedron model and 21.37 m/s with the harmonics model. Figure 4.5 contains the spectral components of the control accelerations. Both models show five noticeable peaks in the X- and Y-control and two in the Z. For this case, the two highest peaks in the X and Y FFTs correspond to the orbit frequency (ω_{orbit} = 1.62E-5 Hz) and twice the asteroid rotation frequency minus three times the orbit frequency ($2\omega_{spin} - 3\omega_{orbit}$ = 5.67E-5 Hz). Increasing or decreasing the orbit radius would change the numerical values of

these numbers, but they remained equal to ω_{orbit} and $2\omega_{spin} - 3\omega_{orbit}$ as long as the result was positive. Figures 4.6 and 4.7 show the results of adding disturbance-accommodating filters of the form given in Equation (3.5) to each of the prominent frequency components. Immediately it can be seen that the control accelerations decrease to near zero, and the bias in both Z-controls was completely eliminated. Both models gave a new ΔV requirement of 0.13 m/s per week. In one iteration, a fuel-efficient controller was able to be designed using this method.

It was mentioned that one of the highest peaks in the X and Y FFT plots corresponded to $2\omega_{spin} - 3\omega_{orbit}$, and that this relation held no matter the orbital radius as long as the resulting frequency was positive. So we will look at a case where the asteroid spin rate and orbit frequency are selected such that $2\omega_{spin} - 3\omega_{orbit} = 0$. Here the orbit frequency remained unchanged but the asteroid spin rate was changed to $\frac{3}{2}\omega_{orbit}$. Figure 4.8 shows the resulting PD control inputs and their corresponding FFT plots. As predicted, the two largest frequencies in the X and Y FFT plots are still ω_{orbit} and $2\omega_{spin} - 3\omega_{orbit}$. The third, smaller frequency is $2\omega_{orbit}$.

4.3 XY-Plane Retrograde Orbit

Next we will examine a similar orbit, except being retrograde instead of prograde. Adding PD control results in a nearly identical ΔV requirement as the prograde case. This would not be obvious by comparing the prograde control acceleration histories in Figures 4.4 to the retrograde ones in Figure 4.9. The Z-axis controls for both retrograde and prograde have about the same amplitude, but the retrograde control oscillates at a higher frequency. On the other hand, the X- and Y-controls for both cases differ greatly from one another both in shape and frequency. This is also reflected in the FFT plots of the prograde orbit in Figures 4.5 and the retrograde orbit in Figure 4.10. While there are about the same number of peaks present, the frequencies tend to be higher in the retrograde case. The largest peak for the retrograde orbit also occurs at a higher frequency than the prograde orbit for each axis control, though the orbit frequency of 1.62E-5 Hz remains a prominent frequency as in the prograde case. After one iteration of adding filters to the FFT frequencies gave a new ΔV requirement of 0.134 m/s per week for the polyhedron model and 0.15 m/s for the harmonic model.

4.4 45° Inclined Orbit

Now we will incline the orbit by 45 degrees to command an orbit that is not in any of the coordinate system planes. When left uncontrolled, an orbit of this type tends to naturally precess about the asteroid, which can be prevented with the addition of PD control at a ΔV expense of 17.65 m/s per week for the polyhedron model and 17.59 m/s for the harmonics model. In this case, the control accelerations along each axis exhibit the same frequency peaks in the FFT plots, though not necessarily with the same magnitude. Of note is that the orbit frequency 1.62E-5 Hz is once again appearing as a prominent peak along all three axes. Filtering these frequencies allows the spacecraft to precess as it would naturally about the asteroid while still being controlled as shown in Figure 4.13. After applying filters to all the frequencies present in Figure 4.15, the control accelerations go to nearly zero, and the ΔV requirement is reduced to 0.123 m/s per week for the polyhedron model and 0.135 m/s per week for the harmonic model.

4.5 Polar Orbit

Perhaps the most useful orbit to command, in terms of scientific return and imaging, would be a polar orbit. Whereas an orbit in the XY-plane would be limited to only viewing parts of the surface in the orbit plane, a polar orbit would be able to view the entire surface due to the spin of the asteroid. Using PD control, we see the most irregular control acceleration history out of the four scenarios (Figure 4.18). While there is still periodicity, the curves for the in-plane controls (X and Z) are not as smooth flowing as those for the inclined, prograde, or retrograde orbits. Despite being the most irregular, this orbit requires the least amount of control effort before applying control filters. The polyhedron model requires 16.85 m/s of ΔV per week, and the harmonic model requires 16.36 m/s. For this orbit, we see the most number of similar sized frequency peaks appear in the FFTs. Applying filters to each of the frequencies present reduces the ΔV per week to 0.112 m/s for the polyhedron model and 0.13 m/s for the harmonics model.

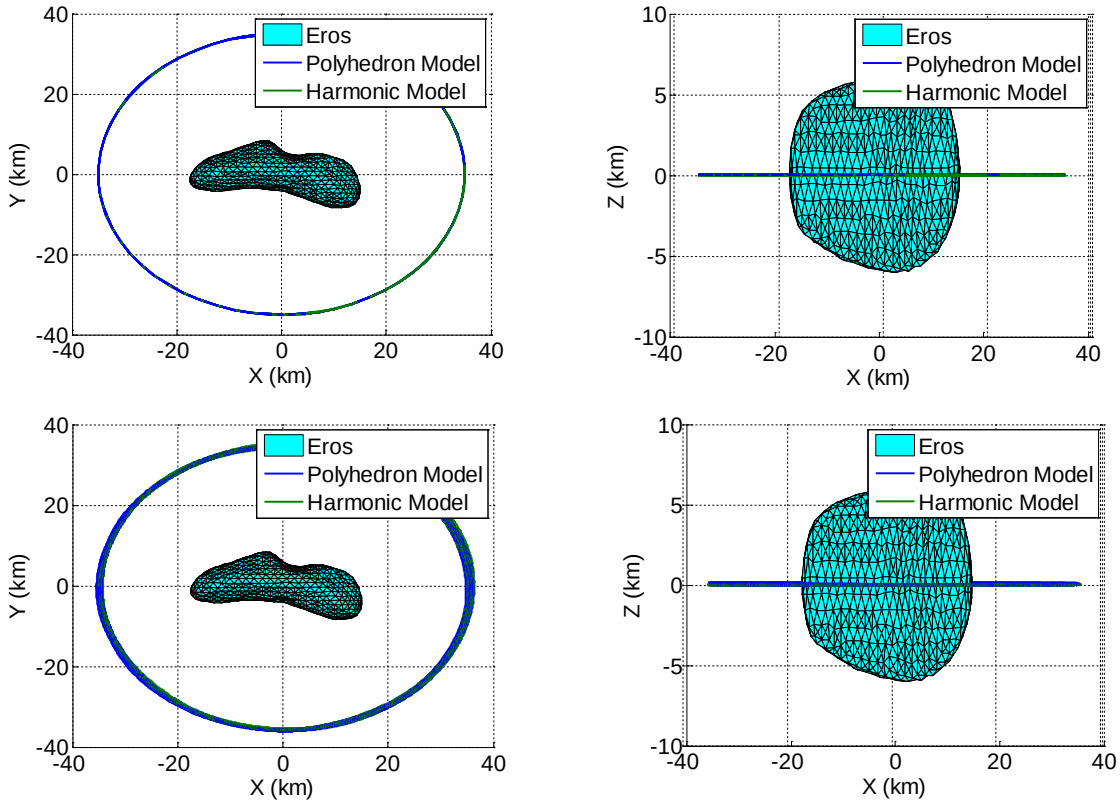

Figure 4.3 35 km prograde orbit with PD control on top and disturbance-accommodating control on the bottom.

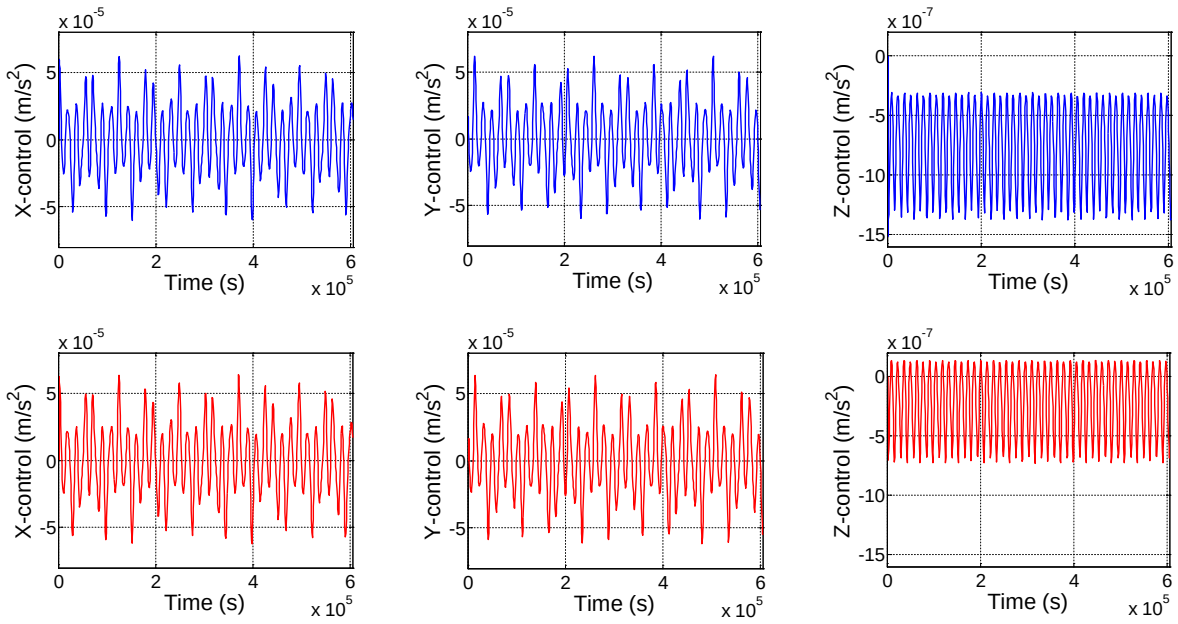

Figure 4.4 35 km prograde orbit control acceleration histories with simple PD control. Polyhedron model on top and the harmonics model on bottom.

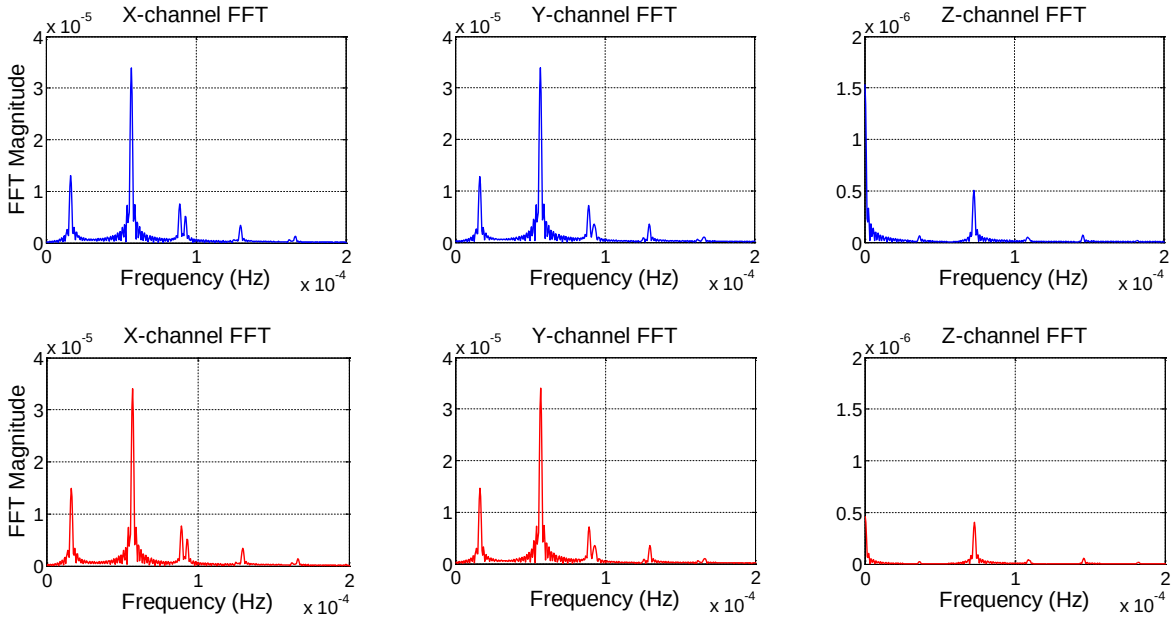

Figure 4.5 FFT plots of the PD control inputs for the 35 km prograde orbit.

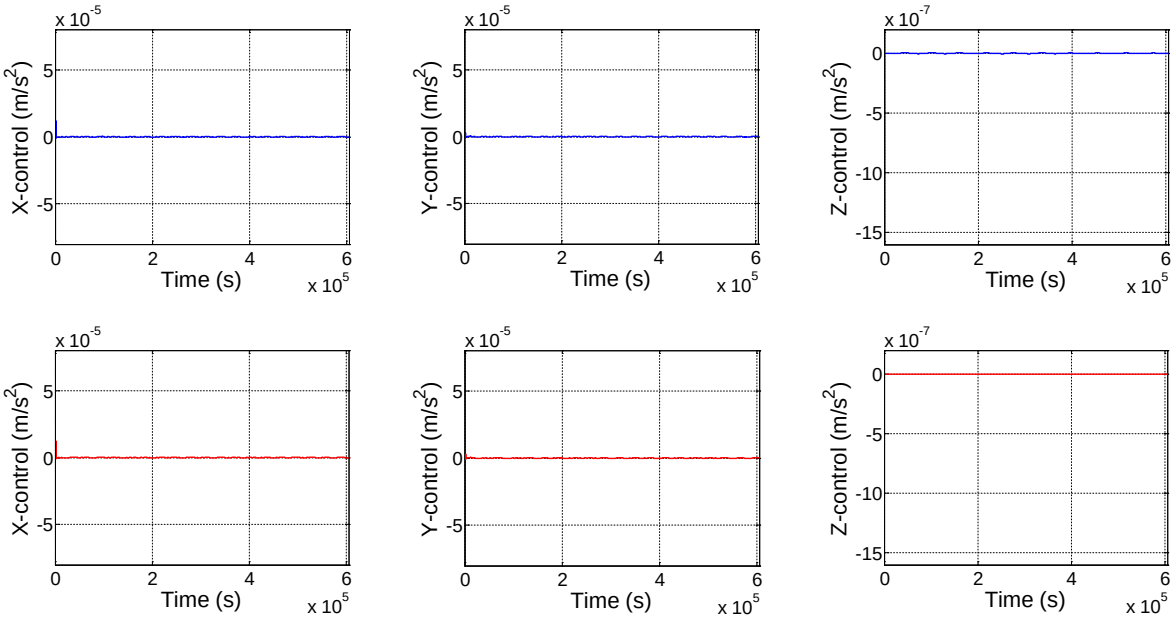

Figure 4.6 35 km prograde orbit control acceleration histories with disturbance-accommodating control. Polyhedron model on top and harmonics model on bottom.

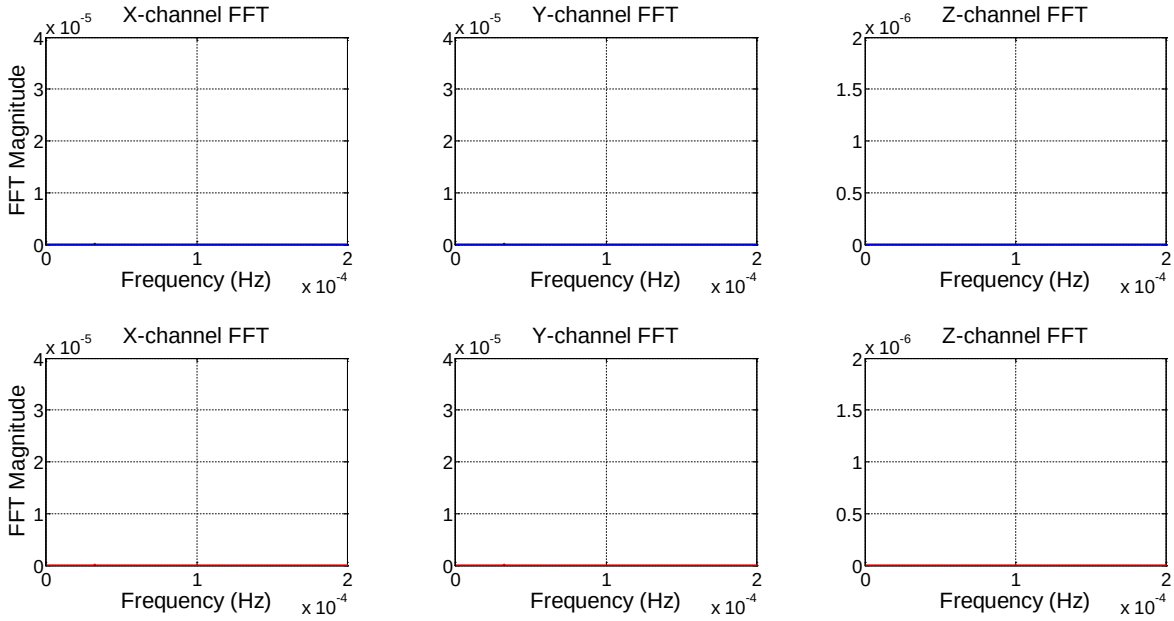

Figure 4.7 FFT plots of the disturbance-accommodating control inputs for the 35 km prograde orbit.

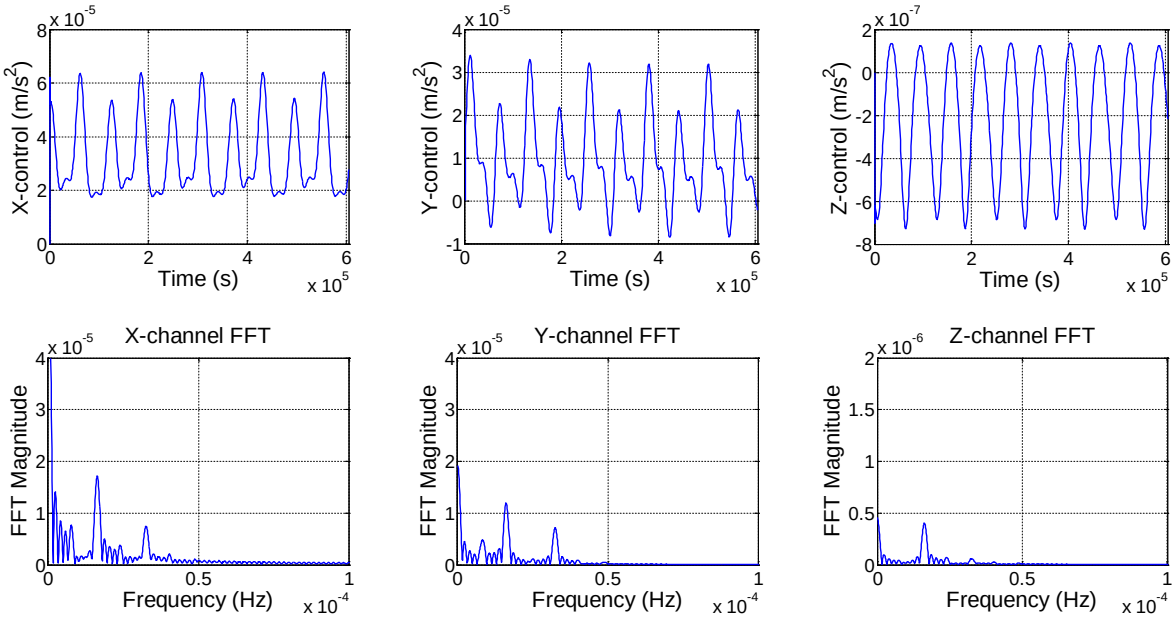

Figure 4.8 PD control inputs and their corresponding FFT plots when $2\omega_{spin} - 3\omega_{orbit} = 0$.

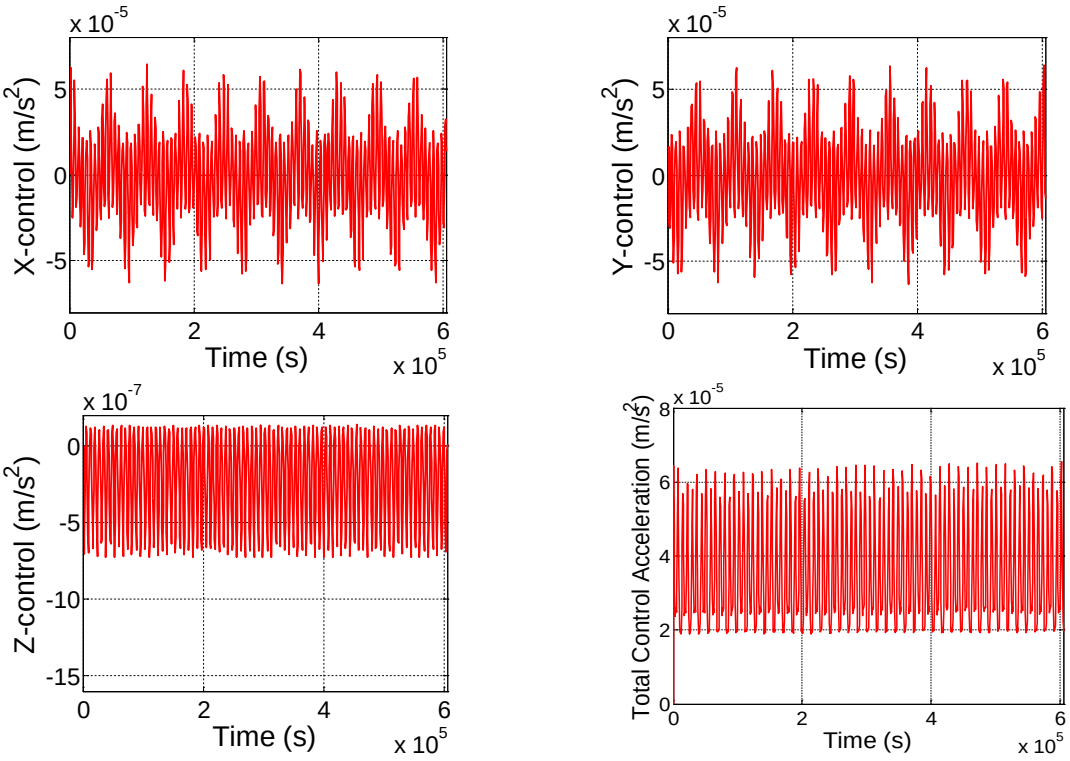

Figure 4.9 35 km retrograde orbit control acceleration histories with PD control.

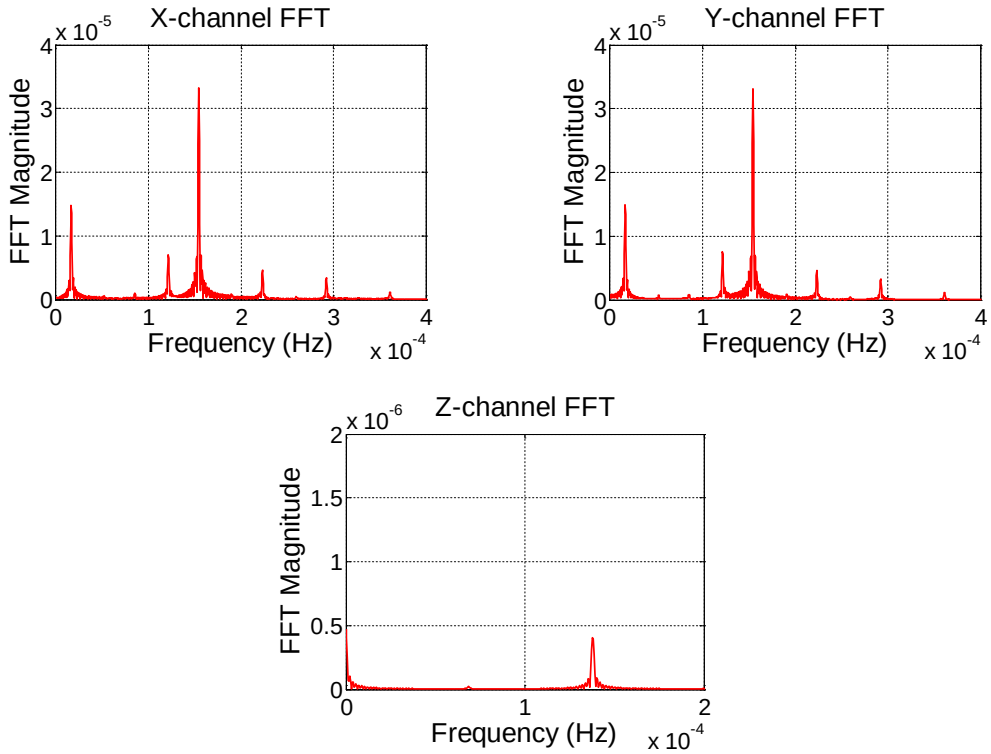

Figure 4.10 FFT plots of the PD control inputs for the 35 km retrograde orbit.

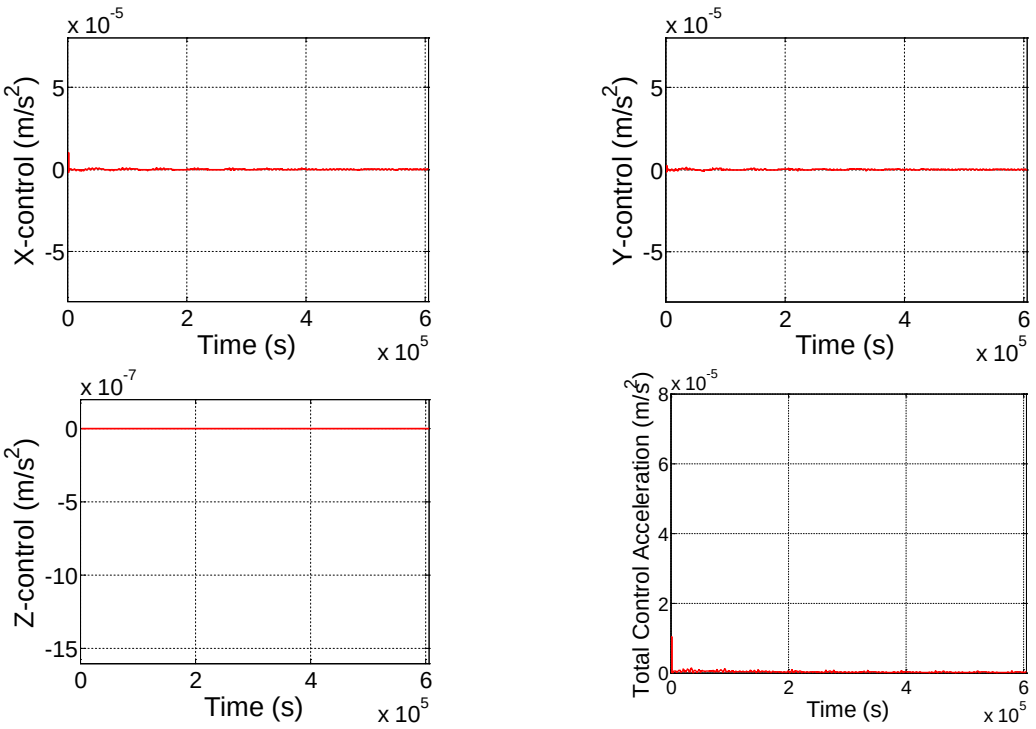

Figure 4.11 35 km retrograde orbit control acceleration histories with disturbance-accommodating control.

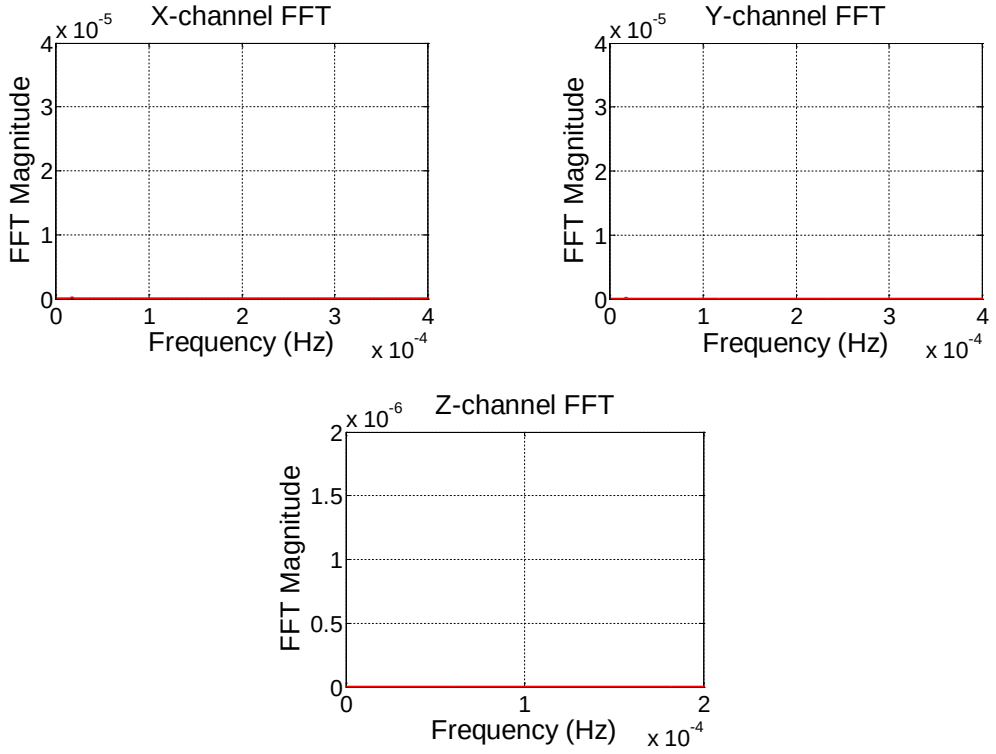

Figure 4.12 FFT plots of the of the disturbance-accommodating control inputs for the 35 km retrograde orbit.

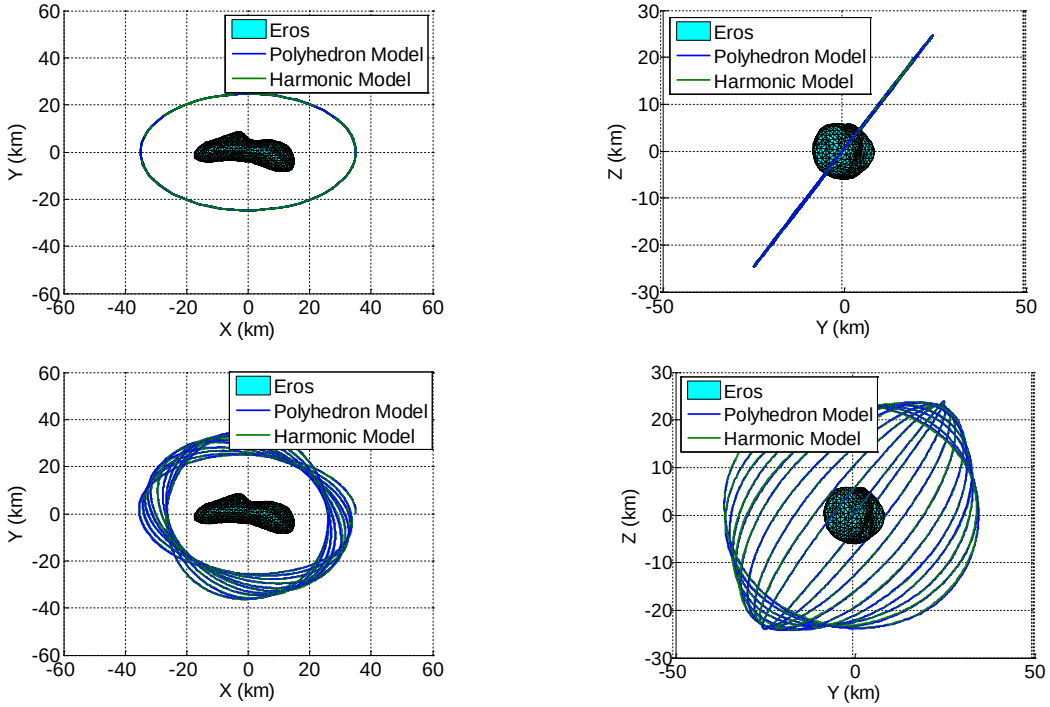

Figure 4.13 35 km inclined orbit with PD control on top and disturbance-accommodating control on the bottom.

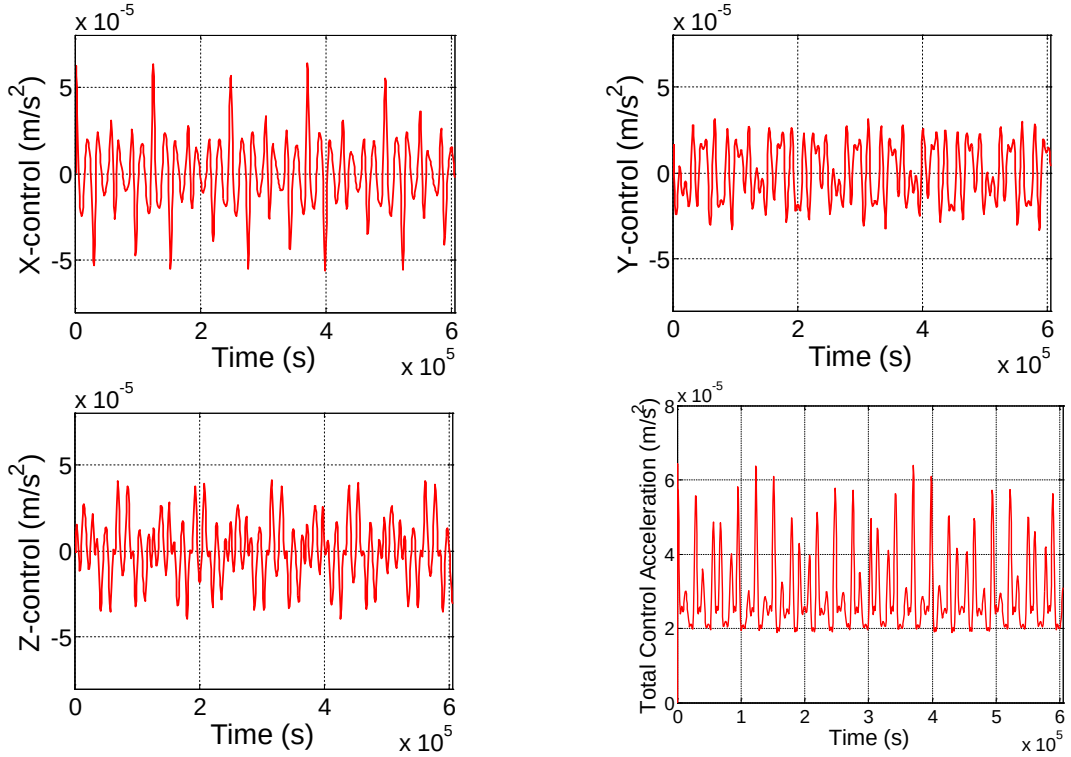

Figure 4.14 Inclined orbit control acceleration histories with PD control.

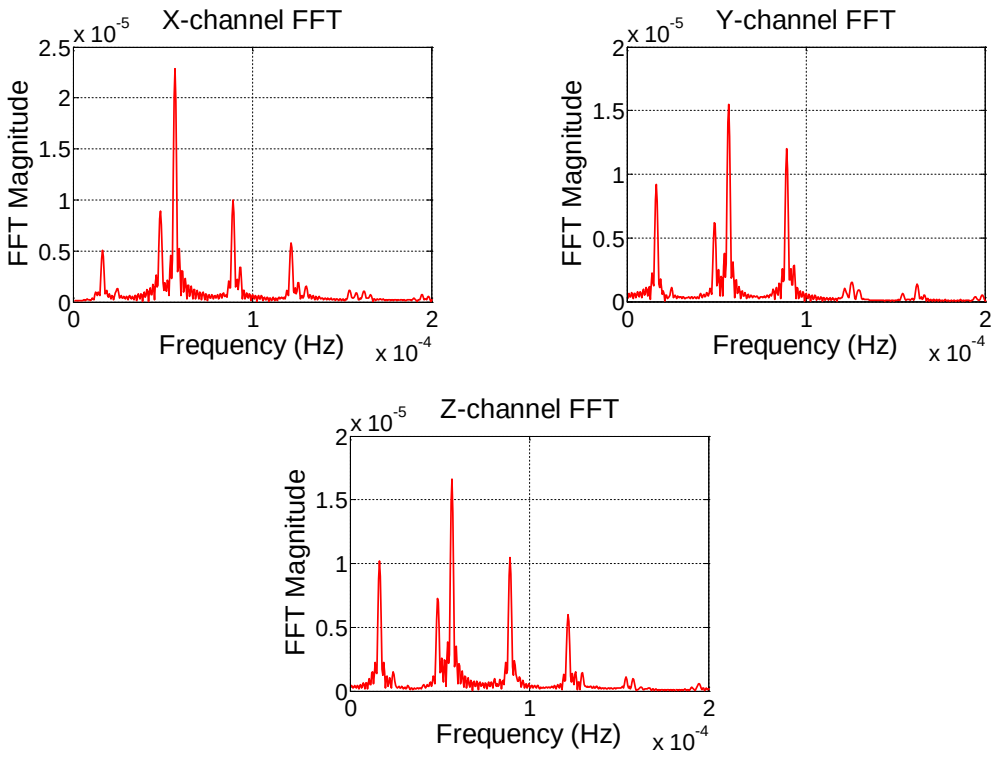

Figure 4.15 FFT plots of the PD control inputs for the inclined orbit.

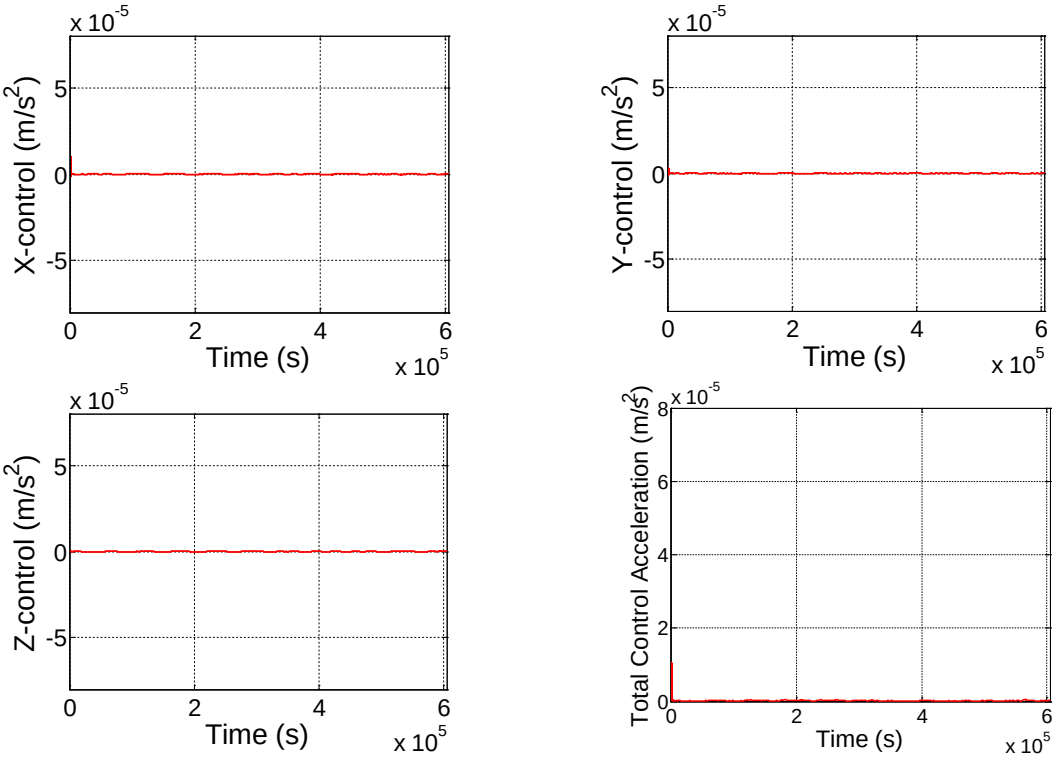

Figure 4.16 Inclined orbit control acceleration histories with disturbance-accommodating control.

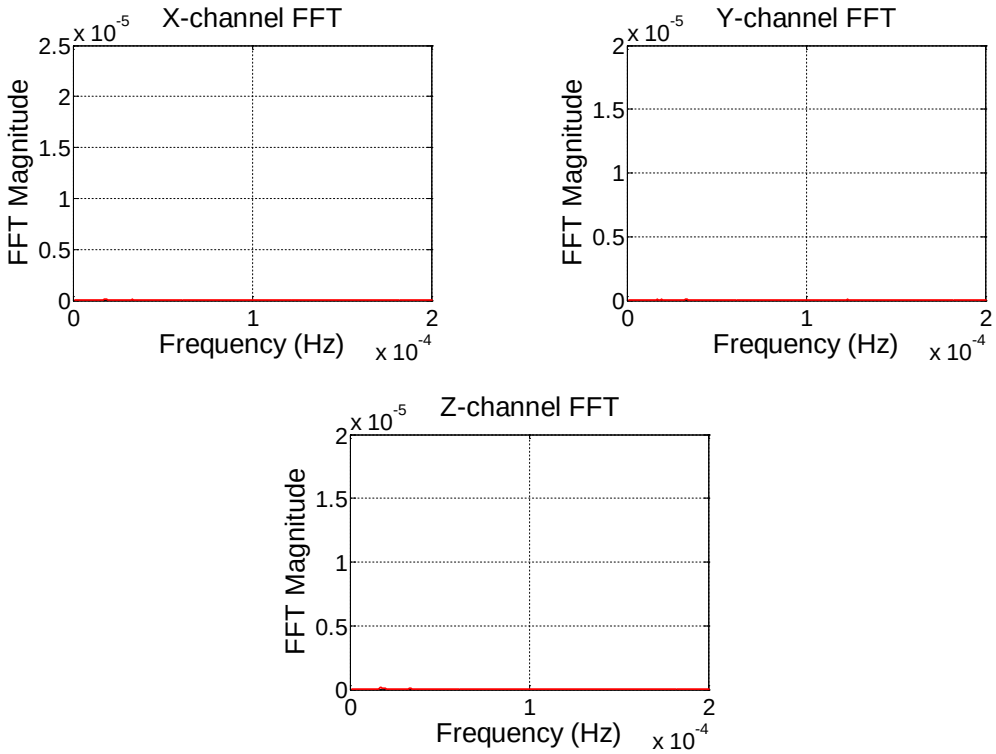

Figure 4.17 FFT plots of the disturbance-accommodating control inputs for the inclined orbit.

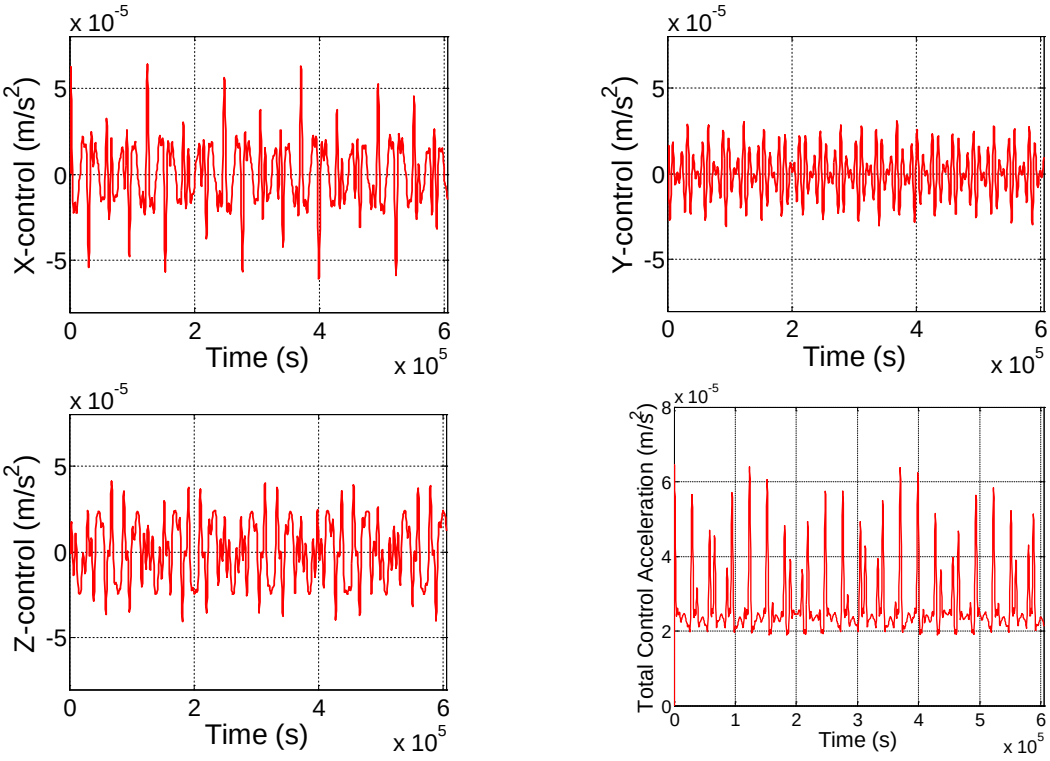

Figure 4.18 Polar orbit control accelerations with PD control.

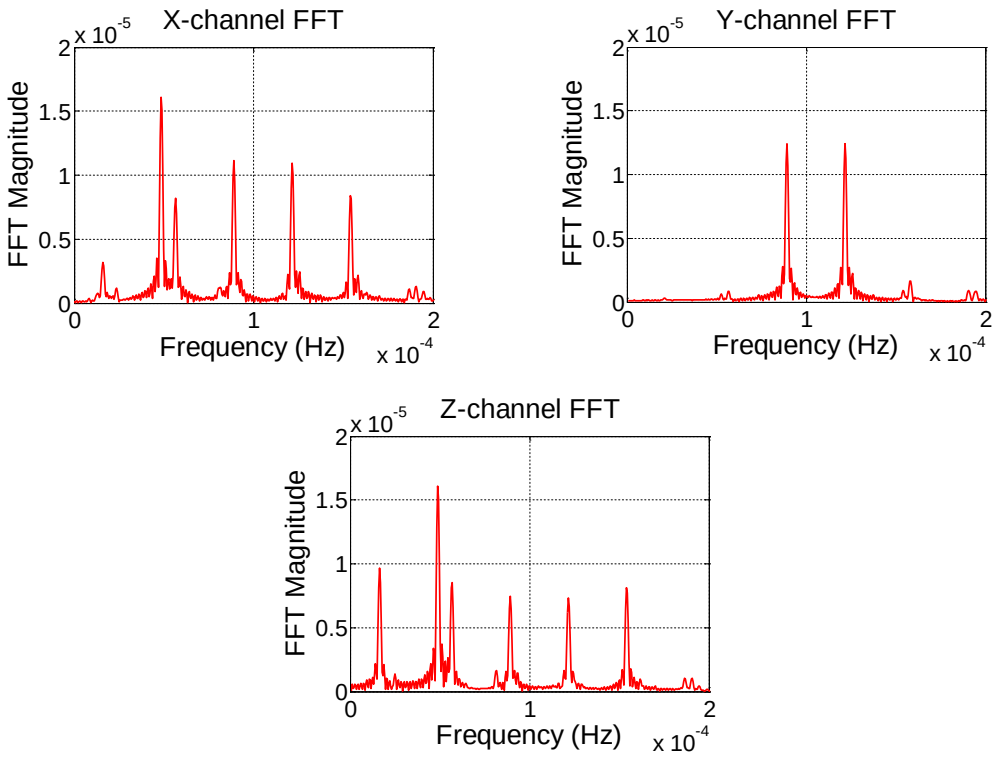

Figure 4.19 FFT plots of the PD control inputs for the polar orbit.

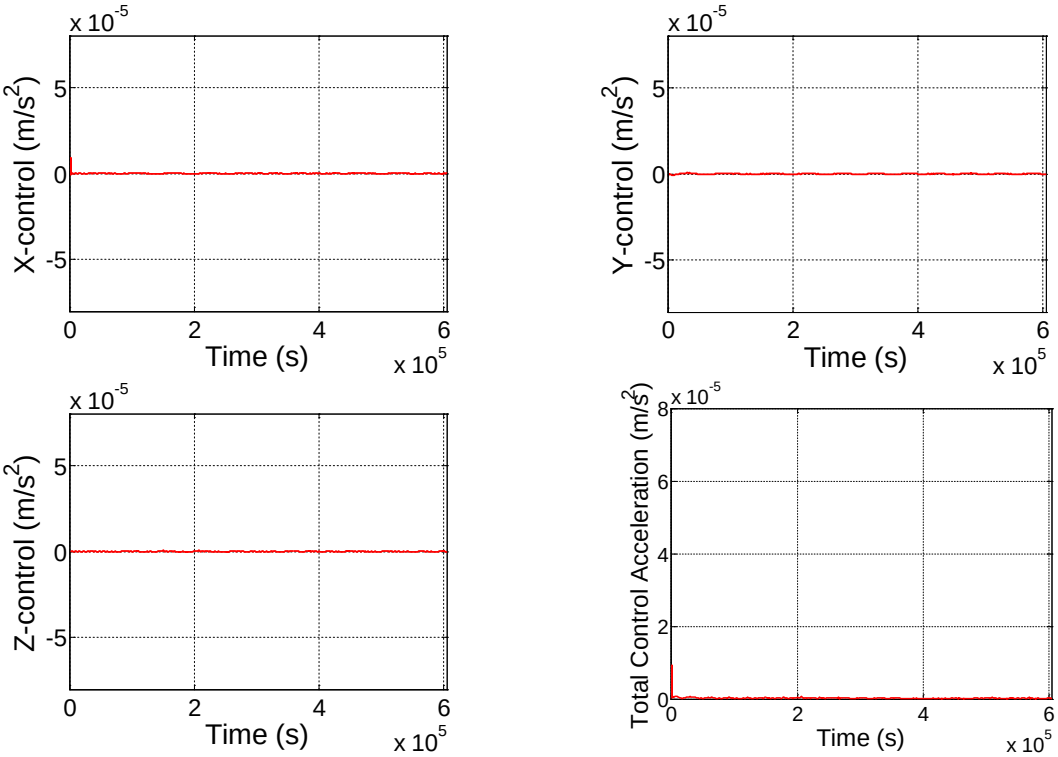

Figure 4.20 Polar orbit control accelerations with disturbance-accommodating control.

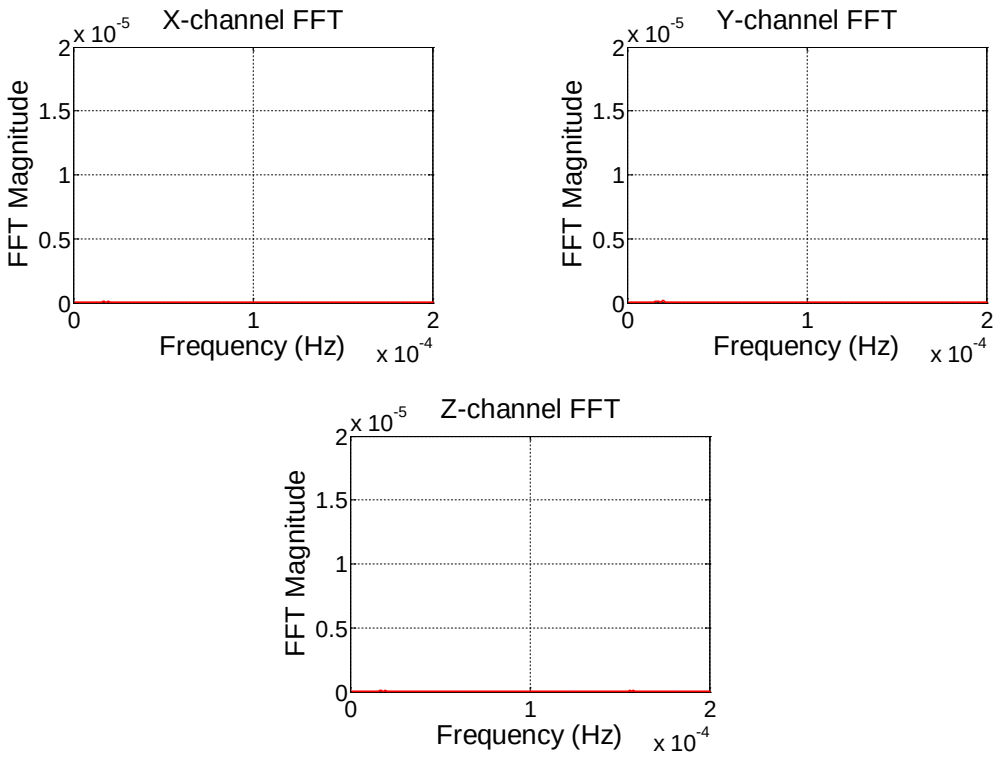

Figure 4.21 FFT plots of the disturbance accommodating-control inputs for the polar orbit.

4.6 Center of Mass Offset

The previous orbiting examples assumed that the asteroid's center of mass (COM) was known with a fair degree of accuracy. Here we test the controller's performance when the COM is incorrectly estimated. First a large, worst-case scenario COM location estimation error of one kilometer is assumed along the negative Z-axis. The spacecraft is then commanded to follow a prograde, 35 km radius circular orbit in the assumed XY-plane around this estimated COM (located at the origin of the coordinate system in Figure 4.22) as done in the previous orbiting scenarios. Using only PD control, the spacecraft is forced to stay in a circular orbit below the true XY-plane with the ΔV requirements being only a few m/s higher than the prograde case around the true COM. Following the usual procedure, the disturbance frequencies are identified from the FFT plots of the control inputs, and used to create a disturbance-accommodating controller. Once implemented, the spacecraft can be seen to oscillate around the true COM located at +1 km along the Z-axis with a ΔV requirement of 0.13 m/s per week. Given the

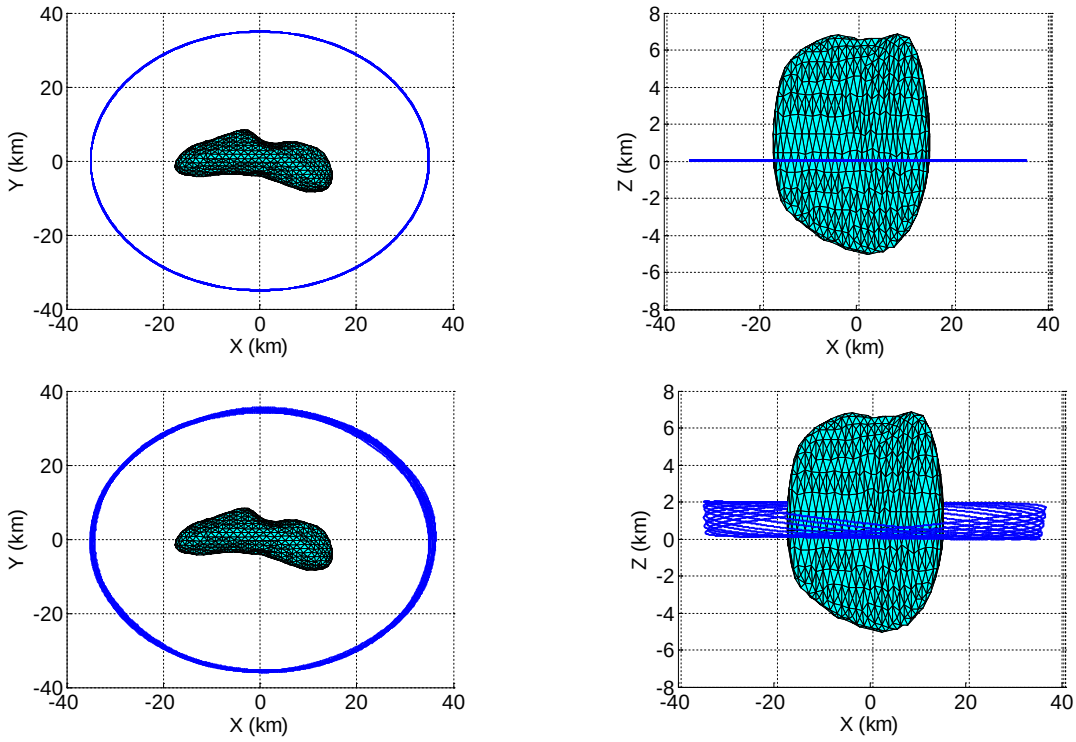

Figure 4.22 Center of mass location error estimation with PD control (top) and disturbance-accommodating control (bottom).

shown robustness of disturbance-accommodating control, the true COM of an asteroid can be estimated with a fair degree of accuracy using this type of control as the controlled stable orbit tends to naturally find this point, and orbit about it.

4.7 Body-Frame Hovering

The last scenario we will examine is hovering in the body-fixed reference frame. Hovering in this case entails finding a reference orbit which has the same period as the asteroid's rotation rate of 5.27 hours. For 433 Eros, the reference circular orbit with the appropriate period is slightly less than 16 km in radius. This radius can be problematic as some dimensions of Eros can also approach 16 km in radius. Thus in order to simulate the hovering case, the spacecraft will have to be placed in areas where the asteroid's radius is significantly smaller such as along the y-axis. As the orbit is slightly less than 16 km, only the polyhedron and inertia dyadic models can be used due to the spherical harmonics unreliability at and below its

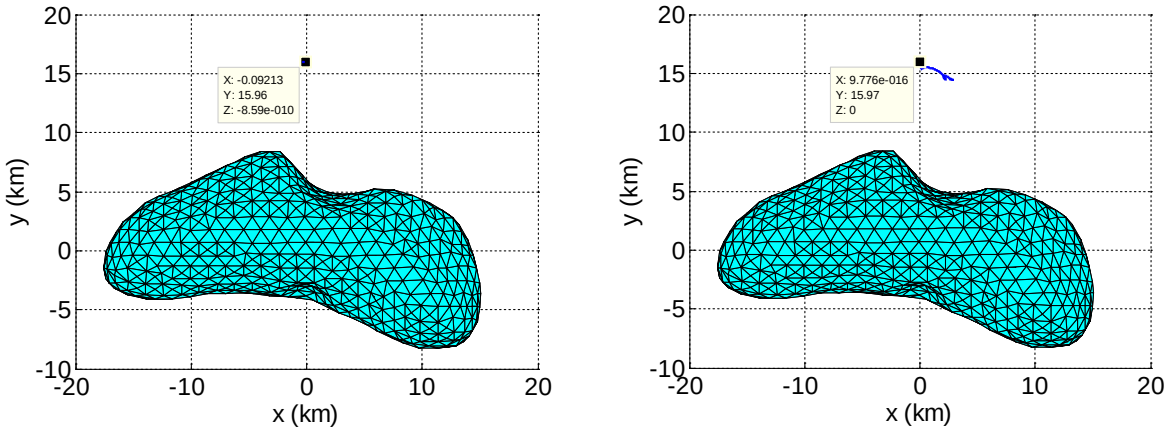

(a) PD control

(b) Disturbance-accommodating control

Figure 4.23 Hovering scenario with PD and disturbance-accommodating control in the body–fixed frame.

minimum circumscribing sphere radius. Since the inertia dyadic model was shown to be similar to a second-order harmonic expansion, the polyhedron shape model will be used instead to obtain more accurate results even though it is computationally slower. Figure 4.23 shows the results of hovering with PD and disturbance-accommodating control in the body-fixed frame. Maintaining the orbit with PD control requires an exorbitant amount of fuel at 199 m/s per week. Here the disturbance-accommodating filters are able to achieve the best reduction yet to 0.5 m/s per week. The large ΔV requirement for PD control appears to be due to the assumed initial position not being close enough to the actual 1:1 orbit as we see the spacecraft position drift significantly in the positive x-direction when control filters are added.

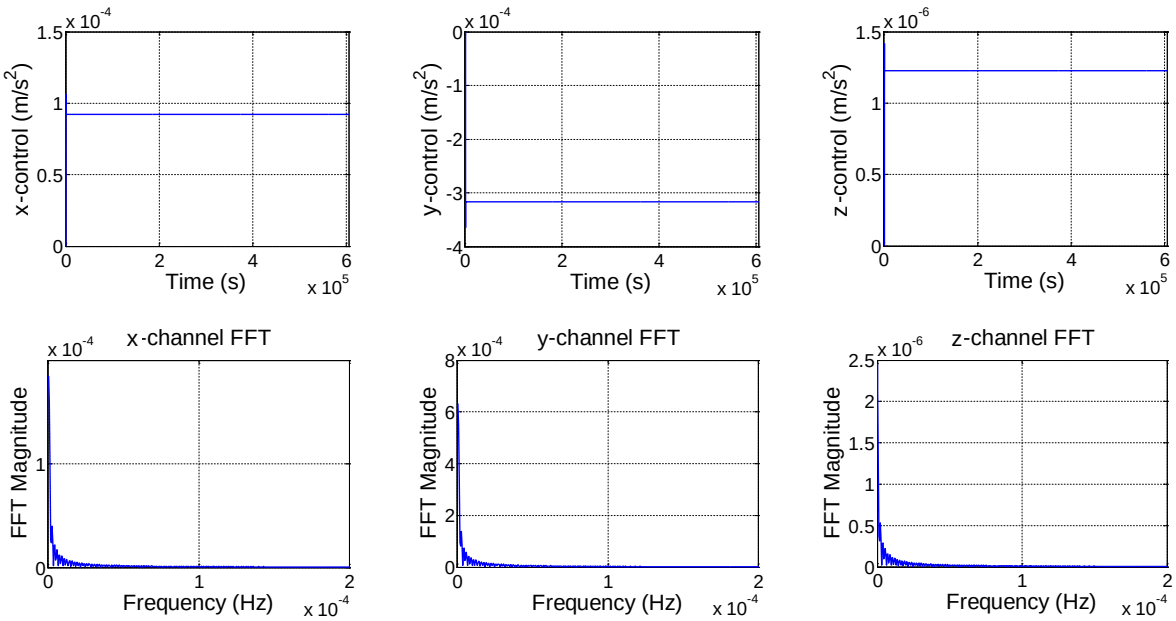

Figure 4.24 Control inputs and their corresponding FFT plots for they hovering scenario in the body-fixed frame.

CHAPTER 5. CONCLUSIONS

This work investigated the orbital control problem of proximity operations around an arbitrarily shaped asteroid incorporating three different models for simulating the weak, non-uniform gravitational fields produced by irregular-shaped bodies. Each of these models was shown to have their advantages and disadvantages from a simulation standpoint. The polyhedron shape model was capable of simulating a gravitational field similar to the more typically used high order spherical harmonic expansion using only the shape of the body and without suffering from regions of invalidity. A drawback of this model is the significantly longer computation time than either the spherical harmonic expansion or inertia dyadic models. It was also demonstrated that a low-order approximation ($\sim 2^{nd}$ order) could be obtained using the inertia dyadic of the gravitating body. This model, though, tends to become inaccurate close to the center of the asteroid body.

Using the developed and tested microgravity environments, the viability and robustness of simple feedback control augmented with disturbance-accommodating filters was then examined. For each of the orbiting scenarios presented, the controller was able to maintain stable orbital motion with very little control effort. In each case except for the body-frame hovering, the ΔV was reduced to between 0.1-0.2 m/s per week. Even then, the hovering case was still able to be reduced from nearly 200 m/s per week to 0.5 m/s. This fuel-efficient control scheme could be used to reduce reliance on ground-based commands, and is more advantageous than open-loop solutions as prior knowledge of the body is not required for implementation. This is due to only needing the control acceleration history to know at which frequencies that control filters should be tuned. The biggest advantage is that we are able to command arbitrary orbits with this form of active control without prior regard to the orbital stability as was necessary in the previous asteroid orbiting operations of NEAR and Dawn.

5.1 Recommendations for Future Work

The current research only included perturbing forces from the asteroid's irregular gravitational field. Future work could incorporate other perturbing forces such as solar radiation pressure in order to increase the accuracy of the dynamical model. Also, the entirety of the control scheme outlined in this work relies on being able to accurately determine a spacecraft's state vector with respect to the asteroid's center of mass. Here the state vector measurements were assumed to be given with a large degree of accuracy in order to verify the validity of this approach. The next logical step could be to integrate optical navigation methods with this control scheme to autonomously estimate the state vector using a combination of data from optical cameras and LIDAR technologies. Both of these devices are already built into most spacecraft, and would realistically simulate the station-keeping activities of an actual deep space exploration mission.

APPENDIX A. SHPERICAL HARMONIC COEFFICIENTS FOR ASTEROID 433 EROS

Table A.1 Normalized spherical harmonic coefficients up to the sixth order and degree [22].

Order	**Degree**	$\bar{C}_{n,m}$	$\bar{S}_{n,m}$
0	0	1	0
1	0	0	0
	1	0	0
2	0	-0.05246	0
	1	0	0
	2	0.08240	-0.02811
3	0	-0.00141	0
	1	0.00406	0.00337
	2	0.00177	-0.00070
	3	-0.01042	-0.01207
4	0	0.01293	0
	1	-0.00010	0.00014
	2	-0.01747	0.00463
	3	-0.00030	-0.00012
	4	0.01746	-0.00911
5	0	0.00066	0
	1	-0.00276	-0.00122
	2	-0.00078	-0.00038
	3	0.00458	0.00354
	4	0.00050	-0.00070
	5	-0.01021	-0.00584
6	0	-0.00498	0
	1	-0.00002	-0.00012
	2	0.00654	-0.00119
	3	0.00029	0.00007
	4	-0.00565	0.00177
	5	-0.00049	0.00005
	6	0.00508	-0.00160

APPENDIX B. INERTIA DYADIC GRAVITATIONAL FORCE DERIVATION [18]

Start at the general equation for gravitational attraction.

$$\vec{F} = -Gm \int \vec{p}(\vec{p}\cdot\vec{p})^{-3/2}\rho dV \tag{B.1}$$

Substitute $\vec{R}+\vec{r}$ in for $\vec{p}$

$$\vec{F} = -Gm \int (\vec{R}+\vec{r})(\vec{R}^2+2\vec{R}\cdot\vec{r}+\vec{r}^2)^{-3/2}\rho dV \tag{B.2}$$

where $\vec{R}^2$ represents $\vec{R}\cdot\vec{R} = |\vec{R}|^2 = R^2$. Now define a vector $\vec{q}$ and the unit vector $\vec{e}_r$ as

$$\vec{q} \equiv \frac{\vec{r}}{R} \qquad\qquad \vec{e}_r = \frac{\vec{R}}{R} \tag{B.3}$$

Substitute Equation B.3 into Equation B.2.

$$\begin{aligned}
\vec{F} &= -Gm \int (R^{-3})(\vec{R}+\vec{r})(1+2\frac{\vec{R}}{R}\cdot\frac{\vec{r}}{R}+\frac{\vec{r}^2}{R^2})^{-3/2}\rho dV \\
&= -\frac{Gm}{R^2} \int (\frac{\vec{R}}{R}+\frac{\vec{r}}{R})(1+2\frac{\vec{R}}{R}\cdot\frac{\vec{r}}{R}+\frac{\vec{r}^2}{R^2})^{-3/2}\rho dV \\
&= -\frac{Gm}{R^2} \int (\vec{e}_r+\vec{q})(1+2\vec{e}_r\cdot\vec{q}+\vec{q}^2)^{-3/2}\rho dV
\end{aligned} \tag{B.4}$$

Assuming $2\vec{e}_r\cdot\vec{q}+\vec{q}^2 < 1$ and using the binomial series expansion

$$(1+x)^n = \sum_{k=0}^{\infty} \frac{n!x^k}{(n-k)!k!} = 1+nx+\frac{1}{2!}n(n-1)x^2+\frac{1}{3!}n(n-1)(n-2)x^3+\ldots \tag{B.5}$$

Equation B.4 becomes

$$\vec{F} = -\frac{Gm}{R^2}\int(\vec{e}_r+\vec{q})[1-\frac{3}{2}(2\vec{e}_r\cdot\vec{q}+\vec{q}^2)+\frac{15}{8}(4(\vec{e}_r\cdot\vec{q})^2+4\vec{q}^2\vec{e}_r\cdot\vec{q}+\vec{q}^4) \\ -\frac{105}{48}(8(\vec{e}_r\cdot\vec{q})^3+12\vec{q}^2(\vec{e}_r\cdot\vec{q})^2)+\ldots]\rho dV \tag{B.6}$$

Expanding and ignoring terms of $\vec{q}^3$ and higher yields

$$\begin{aligned}\vec{F} &= -\frac{Gm}{R^2}\int\{\vec{e}_r[1-\frac{3}{2}(2\vec{e}_r\cdot\vec{q}+\vec{q}^2)+\frac{15}{2}(\vec{e}_r\cdot\vec{q})^2]+\vec{q}[1-3\vec{e}_r\cdot\vec{q}]\}\rho dV \\ &= -\frac{Gm}{R^2}\int\{\vec{e}_r[1-\frac{3}{2}(2\vec{e}_r\cdot\frac{\vec{r}}{R}+\frac{\vec{r}^2}{R^2})+\frac{15}{2}(\vec{e}_r\cdot\frac{\vec{r}}{R})^2]+\frac{\vec{r}}{R}[1-3\vec{e}_r\cdot\frac{\vec{r}}{R}]\}\rho dV \\ &= -\frac{Gm}{R^2}\int\{\vec{e}_r-\frac{3}{R}\vec{e}_r\vec{e}_r\cdot\vec{r}-\frac{3}{2R^2}\vec{e}_r\vec{r}^2+\frac{15}{2R^2}\vec{e}_r\vec{e}_r\cdot\vec{r}\vec{r}\cdot\vec{e}_r+\frac{\vec{r}}{R}-\frac{3}{R^2}\vec{r}\vec{r}\cdot\vec{e}_r\}\rho dV\end{aligned} \tag{B.7}$$

As $\vec{r}$ is taken from the center of mass, the integral $\int\vec{r}\rho dV = 0$ and $\int\rho dV = \bar{m}$

$$\begin{aligned}\vec{F} &= -\frac{G\bar{m}m}{R^2}\vec{e}_r-\frac{3Gm}{2R^4}\int\{-\vec{e}_r\vec{r}^2+5\vec{e}_r\vec{e}_r\cdot\vec{r}\vec{r}\cdot\vec{e}_r-2\vec{r}\vec{r}\cdot\vec{e}_r\}\rho dV \\ &= -\frac{G\bar{m}m}{R^2}\vec{e}_r+\frac{3Gm}{2R^4}\{\vec{e}_r\int\vec{r}^2\rho dV-5\vec{e}_r\vec{e}_r\cdot\int\vec{r}\vec{r}\rho dV\cdot\vec{e}_r+2\int\vec{r}\vec{r}\rho dV\cdot\vec{e}_r\}\end{aligned} \tag{B.8}$$

The relation to the inertia dyadic comes from the definition of the inertia dyad:

$$\widetilde{I} = \int(\widetilde{U}\vec{r}^2-\vec{r}\vec{r})\rho dV \tag{B.9}$$

where $\widetilde{U}$ denotes the unit dyadic. Using the trace operation defined in Equation 2.24, Equation B.9 becomes

$$tr(\widetilde{I}) = \int[tr(\widetilde{U}\vec{r}^2)-tr(\vec{r}\vec{r})]\rho dV = \int(3\vec{r}^2-\vec{r}^2)\rho dV = 2\int\vec{r}^2\rho dV \tag{B.10}$$

Equation B.9 can also be rearranged to yield

$$\int\vec{r}\vec{r}\rho dV = \widetilde{U}\int\vec{r}^2\rho dV-\widetilde{I} = \frac{1}{2}\widetilde{U}\cdot tr(\widetilde{I})-\widetilde{I} \tag{B.11}$$

Substituting Equations B.10 and B.11 into Equation B.8 gives

$$
\begin{aligned}
\vec{F} &= -\frac{G\bar{m}m}{R^2}\vec{e}_r + \frac{3Gm}{2R^4}\{\frac{1}{2}tr(\widetilde{I})\vec{e}_r - 5\vec{e}_r\vec{e}_r\cdot(\frac{1}{2}\widetilde{U}\cdot tr(\widetilde{I}) - \widetilde{I})\cdot\vec{e}_r \\
&+ 2(\frac{1}{2}\widetilde{U}\cdot tr(\widetilde{I}) - \widetilde{I})\cdot\vec{e}_r\} \\
&= -\frac{G\bar{m}m}{R^2}\vec{e}_r + \frac{3Gm}{2R^4}\{\frac{1}{2}tr(\widetilde{I})\vec{e}_r - \frac{5}{2}\vec{e}_r\vec{e}_r\cdot\widetilde{U}\cdot tr(\widetilde{I})\cdot\vec{e}_r + 5\vec{e}_r\vec{e}_r\cdot\widetilde{I}\cdot\vec{e}_r \\
&+ \widetilde{U}\cdot tr(\widetilde{I})\cdot\vec{e}_r - 2\widetilde{I}\cdot\vec{e}_r\} \\
&= -\frac{G\bar{m}m}{R^2}\vec{e}_r + \frac{3Gm}{2R^4}\{\frac{1}{2}tr(\widetilde{I})\vec{e}_r - \frac{5}{2}tr(\widetilde{I})\vec{e}_r + 5\vec{e}_r\vec{e}_r\cdot\widetilde{I}\cdot\vec{e}_r + tr(\widetilde{I})\vec{e}_r - 2\widetilde{I}\cdot\vec{e}_r\} \\
&= -\frac{G\bar{m}m}{R^2}\vec{e}_r + \frac{3Gm}{2R^4}\{-tr(\widetilde{I})\vec{e}_r + 5\vec{e}_r\vec{e}_r\cdot\widetilde{I}\cdot\vec{e}_r - 2\widetilde{I}\cdot\vec{e}_r\} \\
&= -\frac{G\bar{m}m}{R^2}\vec{e}_r - \frac{3Gm}{2R^4}\{tr(\widetilde{I})\vec{e}_r - 5\vec{e}_r\vec{e}_r\cdot\widetilde{I}\cdot\vec{e}_r + 2\widetilde{I}\cdot\vec{e}_r\} \\
&= -\frac{G\bar{m}m}{R^2}[\vec{e}_r + \frac{1}{\bar{m}R^2}\{\frac{3}{2}[tr(\widetilde{I}) - 5\vec{e}_r\cdot\widetilde{I}\cdot\vec{e}_r]\vec{e}_r + 3\widetilde{I}\cdot\vec{e}_r\}] \\
&= -\frac{G\bar{m}m}{R^2}[\vec{e}_r + \vec{f}^{(2)}]
\end{aligned}
\tag{B.12}
$$

Bibliography

[1] Williams, B. G.,et al. Navigation for NEAR Shoemaker: the First Spacecraft to Orbit an Asteroid. In *AAS/AIAA Astrodynamics Specialists Conference*, Quebec City, Quebec, Canada, August 2001. AAS 01-371.

[2] Scheeres, D. J. Orbital Mechanics About Small Bodies. *Acta Astronautica*, 27:1–14, 2012.

[3] Holdridge, M. E. NEAR Shoemaker Spacecraft Mission Operations. *Johns Hopkins APL Technical Digest*, 23(1):58–70, 2002.

[4] Dunham, D. W., McAdams, J. V., and Farquhar, R. W. NEAR Mission Design. *Johns Hopkins APL Technical Digest*, 23(1):18–33, 2002.

[5] Russel, C. T., et al. Dawn Mission and Operations. In *Proceedings International Astronomical Union Symposium: Asteroids, Comets, Meteors*, Rio de Janeiro, Brazil, August 2005.

[6] Broschart, S. B. and Scheeres, D. J. Control of Hovering Spacecraft Near Small Bodies: Application to Asteroid 25143 Itokawa. *Journal of Guidance, Control, and Dynamics*, 27(2):343–354, 2005.

[7] Kawaguchi, J. Hayabusa, Summary of Guidance, Navigation, and Control Achievement in its Proximity Phase. In *AAS/AIAA Astrodynamics Specialist Conference*, Keystone, CO, August 2006. AIAA Paper 2006-6533.

[8] Scheeres, D. J. Dynamics About Uniformly Rotating Tri-Axial Ellipsoids: Applications to Asteroids. *Icarus*, 110:225–238, 1994.

[9] Scheeres, D. J., Ostro, S. J., Hudson, R. S., and Werner, R. A. Orbits Close to Asteroid 4769 Castalia. *Icarus*, 121:67–87, 1996.

[10] Scheeres, D. J, Williams, B. G., and Miller, J. K. Evaluation of the Dynamic Environment of an Asteroid: Applications to 433 Eros. *Journal of Guidance, Control, and Dynamics*, 23:466–745, 2000.

[11] Hu, W. and Scheeres, D. J. Numerical Determination of Stability Regions for Orbital Motion in Uniformly Rotating Second Degree and Order Gravity Fields. *Planetary and Space Science*, 52:685–692, 2004.

[12] Hu, W. and Scheeres, D. J. Periodic Orbits in Rotating Second Degree and Order Gravity Fields. *Chinese Journal of Astronomy and Astrophysics*, 8(1):108–118, 2008.

[13] Scheeres, D. J. Satellite Dynamics About Small Bodies: Average Solar Radiation Pressure Effects. *Journal of Astronautical Sciences*, 47(1):25–46, 1999.

[14] Scheeres, D. J. and Marzari, F. Spacecraft Dynamics in the Vicinity of a Comet. *Journal of the Astronautical Sciences*, 50(1):35–52, 2002.

[15] Scheeres, D. J., Miller, J. K., and Yeomans, D. K. The Orbital Dynamics Environment of 433 Eros: A Case Study for Future Asteroid Missions. Interplanetary network progress report 42-152, 2003.

[16] Werner, R. A. and Scheeres, D. J. Exterior Gravitation of a Polyhedron Derived and Compared with Harmonic and Mascon Gravitation Representations of Asteroid 4769 Castalia. *Celestial Mechanics and Dynamical Astronomy*, 65:313–344, 1997.

[17] Vallado, D. A. *Fundamentals of Astrodynamics and Applications*. Microcosm Press and Springer, 2007.

[18] Kane, T. R., Likins, P. W., and Levinson, D. A. *Spacecraft Dynamics*. McGraw-Hill Book Company, 1983.

[19] Sincarsin, G. B. and Huges, P. C. Gravitational Orbit-Attitude Coupling for Very Large Spacecraft. *Celestial Mechanics and Dynamical Astronomy*, 31(2):143–161, 1983.

[20] Miller, J. K., et al. Determination of Eros Physical Parameters for Near Earth Asteroid Rendezvous Orbit Phase Navigation. Girdwood, AK, 1999. AAS/AIAA Astrodynamics Specialist Conference. Paper AAS 99-463.

[21] Miller, J. K., et al. Determination of Shape, Gravity, and Rotational State of Asteroid 433 Eros. *Icarus*, 155:3–17, 2002.

[22] NEAR-A-5-COLLECTED-MODELS-V1.0. http://sbn.psi.edu/pds/resource/nearbrowse.html.

[23] Cielaszyk, D. and Wie, B. New Approach to Halo Orbit Determination and Control. *Journal of Guidance, Control, and Dynamics*, 19(2):266–273, 1996.

[24] Wie, B. *Space Vehicle Dynamics and Control*. American Institute of Aeronautics and Astronautics, 2008.

[25] Johnson, M. A. Recent Trends in Linear Optimal Quadratic Multivariable Control System Design. *Control Theory and Applications*, 134(1):53–71, 1987.

[26] Robandi, I., Nishimori, K., Nishmura, R., and Ishihara, N. Full-Element Weighting Matrices Q and R Design in Optimal Load Frequency Control Solution Using Genetic Algorithm. In *International Conference on Soft Computing*, Iizuka, Japan, October 2000.

[27] Robandi, I., Nishimori, K., Nishimura, R., and Ishihara, N. Optimal Feedback Control Design Using Genetic Algorithm in Multimachine Power System. *International Journal of Electrical Power and Energy Systems*, 23:263–271, 2001.